In situ fragmentation of Al/Al2O3 multilayers on flexible substrates in biaxial tension

Barbara Putz, Thomas E.J. Edwards, Emese Huszar, Laszlo Pethö, Patrice Kreiml, Megan Cordill, Dominique Thiaudiere, Stephane Chiroli, Fatih Zighem, Damien Faurie, et al.

Materials & Design 232 (2023) 112081

Contents lists available at ScienceDirect

Materials & Design

journal homepage: www.elsevier.com/locate/matdes

In situ fragmentation of Al/Al_2O_3 multilayers on flexible substrates in biaxial tension

Barbara Putz [a,b,*], Thomas E.J. Edwards [a], Emese Huszar [a], Laszlo Pethö [a], Patrice Kreiml [b,c], Megan J. Cordill [c], Dominique Thiaudiere [d], Stephane Chiroli [e], Fatih Zighem [e], Damien Faurie [e], Pierre-Olivier Renault [f], Johann Michler [a]

[a] Empa, Swiss Federal Laboratories for Materials Science and Technology, Thun, Switzerland
[b] Department of Materials Science, Montanuniversität Leoben, 8700 Leoben, Austria
[c] Erich Schmid Institute of Materials Science, Austrian Academy of Sciences, Leoben, Austria
[d] Synchrotron SOLEIL, L'Orme des Merisiers, Saint-Aubin, France
[e] LSPM-CNRS, Université Sorbonne Paris Nord, 93430 Villetaneuse, France
[f] Pprime Institute, CNRS-University of Poitiers, France

HIGHLIGHTS

- Unique Al/Al_2O_3 multilayers produced by combining atomic layer and physical vapor deposition without breaking vacuum.
- Deformation behavior investigated *in situ* in biaxial tension with Synchrotron X-ray diffraction on polymer substrates.
- Observed weakening of Al layers with increasing oxide thickness (0.14–9.4 nm) in contrast to uniaxial tensile results.
- FE model of TEM cross-sections shows strain heterogeneities induced by wavy interfaces and a high young's modulus contrast.
- Model describing the full biaxial yield surface of the multilayers appears to be valid up to 2.4 nm oxide thickness.

GRAPHICAL ABSTRACT

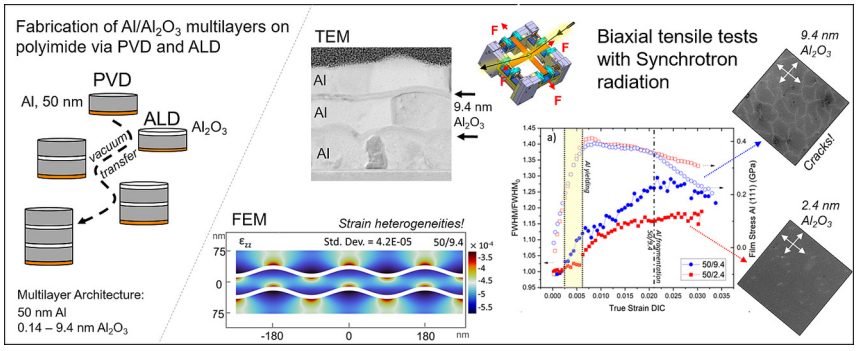

ARTICLE INFO

Article history:
Received 13 April 2023
Revised 6 June 2023
Accepted 7 June 2023
Available online 12 June 2023

Keywords:
Al – Al_2O_3 multilayers
X-ray Diffraction
Flexible Substrates
Mechanical Properties
Fragmentation

ABSTRACT

A unique deposition approach combining atomic layer deposition (ALD) and magnetron sputtering was used to fabricate a series of thin film multilayer structures of Al (50 nm) and Al_2O_3 (ALD, 2.4–9.4 nm) on flexible polymer substrates without breaking vacuum. The multilayers together with 50 nm and 150 nm Al reference films were analyzed by cross-sectional TEM analysis and experimentally strained in biaxial tension to investigate their deformation behavior. Al film stresses and peak widths, measured *in situ* with Synchrotron X-ray diffraction, are in good agreement with post-mortem surface SEM and through-thickness FIB analysis of the multilayers. It was revealed that brittle cracking of the multilayer can be avoided, and that the lateral and through-thickness crack resistance improve as a function of decreasing oxide layer thickness. An attempt to model the full biaxial yield surface of the multilayers, which remains experimentally challenging, appears to be valid up to 2.4 nm oxide thickness. Model predictions are further compared to compression data, obtained from the unloading segments of the tensile

* Corresponding author at: Empa, Swiss Federal Laboratories for Materials Science and Technology, Thun, Switzerland.
E-mail address: barbara.putz@empa.ch (B. Putz).

https://doi.org/10.1016/j.matdes.2023.112081

Tensile Testing

tests. Describing the mechanical behaviour under multiaxial stress conditions is of utmost importance for a diverse understanding of these multilayers across a variety of potential carrier systems and loading cases.

1. Introduction

Nano multilayers and laminates constitute unparalleled model materials to study length-scale dependent deformation mechanisms. They are also highly technologically relevant, with promising mechanical and functional properties, suitable for a wide range of applications with challenging thermal, mechanical or environmental conditions [1]. Multilayer systems are typically classified with respect to the type of materials combined (metal/metal [2-4], metal/ceramic [5,6], ceramic/ceramic [7]) or the microstructure of individual layers (crystalline/amorphous, crystalline/crystalline, amorphous/amorphous) and interfaces [8] (coherent, semi-coherent, incoherent). For metal/ceramic multilayers, subject of this work, an enhancement in both multilayer hardness and ductility compared to the rule of mixture values has been shown experimentally [5,8-16] and through simulations [5,8,17-20], depending on the bilayer thickness, the thickness ratio between ceramic and metal layers, and interfacial properties [5,8]. At the micron scale (25 μm total thickness), nanolayered Al/Al_2O_3 in particular has been suggested for applications requiring a combination of low friction coefficient, high wear resistance and hardness [21]: a systematic increase in wear resistance is observed with decreasing layer thickness, with a drop of 70 % in the peak friction coefficient with optimal layer thicknesses (200 nm Al). In the thin film form and on polymeric substrates, potential applications range from (flexible) microelectronics to satellite insulation [22,23] as the multilayer/polymer composites combine desirable mechanical and functional properties: higher strength, good conductivity, and crack resistance due to sublayer fragmentation and crack deflection at interfaces. Nano-layered composites of metal (Cu, Ni) and graphene exhibit ultra-high strength in nanopillar compression test [9] and a 5–6 times enhanced fatigue resistance compared to the conventional Cu thin film in cyclic bending experiments [24].

Under load, metal layers with a thickness > 10 nm can undergo elastic–plastic deformation while the ceramic layers deform elastically until failure through cracking [12], while at a reduced layer thickness of a few nanometers, ultra-thin ceramics can plastically co-deform with the metal, as has been shown for Al/TiN [12,19]. Substantial intrinsic ductility of amorphous oxides (Al_2O_3) at small scales has also been demonstrated for single layers [25] and within multilayer stacks [16,26], provided that the material is dense and free of geometrical flaws. An effective alternative to nanoindentation [27] or micro pillar compression [16] of substrate supported multilayers or experimentally challenging tensile testing of free-standing films [28] is the use of flexible polymer substrates [29-31], with the advantage of easier sample handling and facilitated mechanical characterization of systems with a low total thickness. Commonly, *ex situ* or *in situ* uniaxial tensile tests and fragmentation analysis are performed on polymer-supported thin films, recording the evolution of cracks and buckles in the film as a function of applied load [30-32], whereby microscopic analysis has been extended by *in situ* sensing of functional properties such as electrical resistance [33] and magnetic properties [34,35] or film stresses by X-ray diffraction [29,36-41]. It is important to note here that in most cases uniaxial tensile testing of polymer-supported thin films results in a biaxial stress state in the film, due to and depending on the Poisson ratio difference ($\Delta\nu$) between film and substrate. This generally requires film stress measurements parallel and perpendicular to the tensile direction to determine the complete stress state [36,37,41] and can result in tensile induced delamination (buckling [42]). Solutions for more complex and application relevant loading conditions include various bending setups [43,44], bulge testing [45-49] and complex 2D tensile machines [50-53]. The latter one is scarcer due to more complex instrumentation, but unique in its capability to vary the loading ratio in a controlled manner, which revealed that film stress evolution, crack initiation and multiplication differ for the uni- vs. biaxial loading case [50]. Another strong argument for much-needed multiaxial characterization, particularly considering multilayers and nanolaminates, are observations that deformation properties of materials under multiaxial loading conditions and different loading ratios are different than those predicted by uniaxial tests [54-56].

In this work we report biaxial tensile testing with *in situ* X-ray diffraction (XRD) and post-mortem lateral and through-thickness fragmentation analysis of crystalline metal/amorphous oxide (Al/Al_2O_3) nanolaminates on flexible polyimide substrates. Polyimide is a high temperature capable polymer with good adhesion to metallic coatings [57]. Combining metal layers with their natural oxide results in excellent adhesion between the individual layers, reducing the risk of spontaneous delamination, and ensuring the structural integrity of the multilayer system [58]. Film stress evolution as well as the width of the Bragg reflection, reflecting intra-phase strain heterogeneity, both give information on the different deformation mechanisms in crystalline layers [50]. Additionally, conclusions about oxide layer fracture can be drawn via the known phenomenon, describing how cracks in the brittle layers cause stress concentration and through-thickness fracture of ductile layers at very low strains (1–2%) [37,59,60]. Mechanical characterization of ultrathin oxides remains extremely challenging, also due to electron beam assisted plasticity effects [61]. Our films are produced by a unique approach combining atomic layer deposition (ALD) and physical vapor deposition (PVD, magnetron sputtering) without breaking vacuum. With a minimum layer thickness of 0.14 nm for Al_2O_3, this process far exceeds the thickness restrictions of natural oxidation of Al (2–10 nm [62-64]), and importantly the commonly investigated modulation and thickness ratios of metal/ceramic multilayer films. In a recently published uniaxial test campaign [26], such multilayers show improved strength and good crack resistance up to an oxide thickness of 2.4 nm. We integrate the results of this biaxial study with recent uniaxial results in an attempt to assess the complete biaxial stress dependence of plasticity [65] and develop a comprehensive description of the mechanical behavior and crack resistance of these metal/oxide multilayers.

2. Experimental

Al/Al_2O_3 multilayers were deposited onto 50 μm thick polyimide (PI, Upilex-S) and Si substrates through alternating cycles of magnetron sputtering (PVD) and ALD without breaking vacuum. The schematics in Fig. 1a-b show the two halves of the combined deposition approach, PVD and ALD, respectively, and Fig. 1c the evolution of the resulting multilayer structure. The custom-made combined ALD/PVD deposition chamber (Mantis Deposition Ltd.,

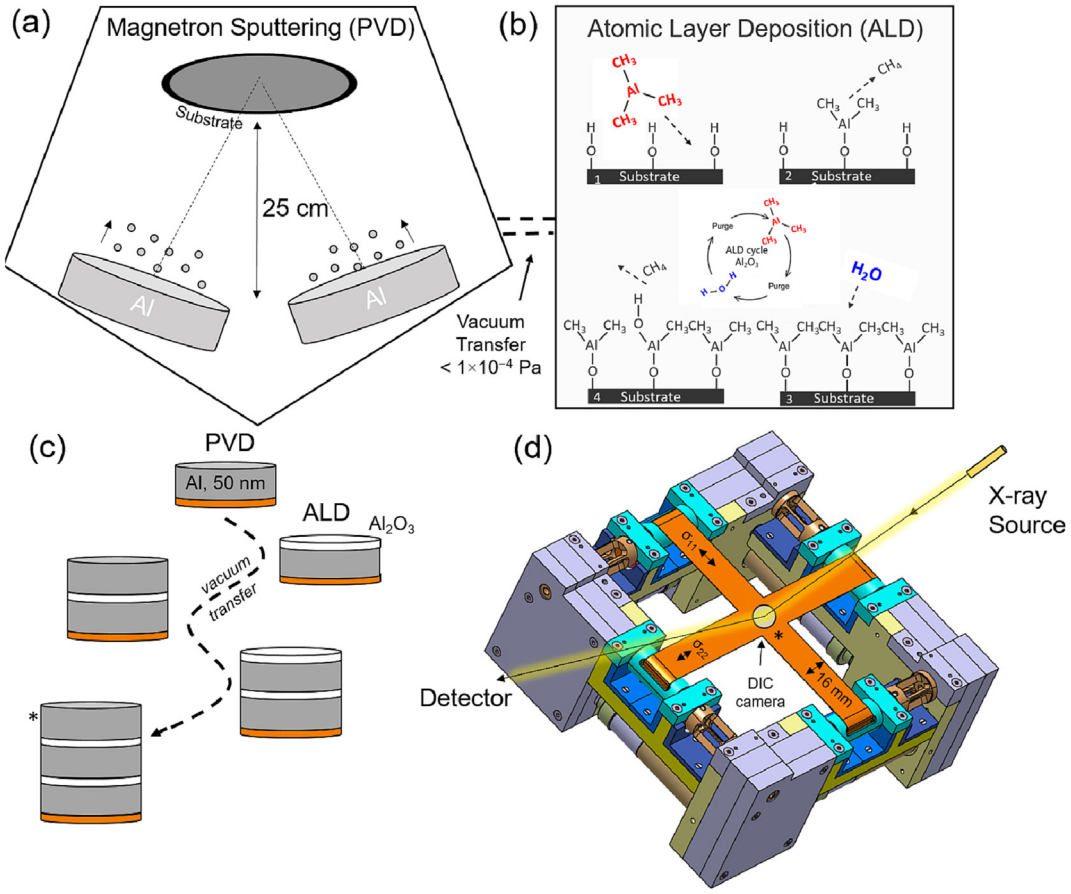

Fig. 1. Multilayer deposition and mechanical testing. a-b) Schematic representations of the two halves of the combined deposition approach PVD and ALD, respectively. c) Evolution of the resulting thin film multilayers. d) Schematic of the biaxial tensile setup with correlated in-situ XRD and DIC measurements.

based on model: QPrep500, UK) is described in detail in [66]. The polymer substrates were pre-cut into cruciform shapes with an arm width of 16 mm, and ultrasonically cleaned with Acetone and Isopropanol prior to deposition. As part of the chamber preheating for the ALD process substrates of the multilayer samples were kept at elevated temperatures (ca. 8 h, 100 °C, UHV) prior to deposition. The reference Al samples were deposited without substrate preheating. A mask was used to deposit thin film circles (diameter 12 mm) in the center of each crucible, avoiding post-deposition etching steps and edge effects during mechanical testing [51]. Al layers with a nominal thickness of 50 nm and 150 nm were magnetron sputtered from two Al targets (purity 99.99%, 76.2 mm diameter) equidistant from the substrate table without substrate rotation. Sputter parameters include a current of 150 mA, a base pressure of 7×10^{-7} mbar, a working pressure of 5×10^{-3} mbar (Ar) and a combined deposition rate of 0.05 nm/s.

Intermediate ALD of Al_2O_3 was performed at about 120 °C with a precursor sequence of pulse-exposure-purge-evacuation-purge at 0.5–1-30–40-10 s for trimethylaluminium (TMA) and 0.5–1-6 0–80-10 s for H_2O. TMA and H_2O were kept at room temperature, with Ar used as the carrier and purging gas. These deposition conditions resulted in amorphous and stoichiometric Al_2O_3 layers with an average growth per cycle (GPC) of approximately 0.14 nm as reported in [66]. The following nominal oxide thicknesses were deposited by adjusting the number of ALD cycles: 67 cycles – 9.4 nm, 17 cycles – 2.4 nm, 1 cycle – 0.14 nm. In total, three Al/Al_2O_3 multilayer structures were created: 50/9.4/50/9.4/50, 50/2.4/50/2.4/50, 50/1cycle/50/1cycle/50 (in nm), along with pure 50 nm and 150 nm Al references. The multilayers will be referred to as 50/9.4, 50/2.4 and 50/1cycle throughout the manuscript. Focused ion beam (FIB, FEI Helios NanoLab Dualbeam, USA) prepared liftouts were investigated with transmission electron microscopy (TEM, Jeol JEM 2200 fs, Japan). Thicknesses and microstructure of individual PVD layers were confirmed via bright field scanning cross-sectional imaging (BF-STEM). For ALD layers high resolution cross-sectional imaging (HR-TEM) was performed.

All samples were continuously loaded in tension with in-plane quasi-equibiaxial strain to about 3.5% (principles strains ratio $\varepsilon_1/\varepsilon_2 \sim 1.3 \pm 0.10$, scattering vector Q perpendicular to loading axis σ_{11}) and unloaded with a strain rate of 7×10^{-6}/s at the DiffAbs beam line of the synchrotron radiation facility SOLEIL [65] following a similar procedure as described in Ref. [50]. Principle strain (ε_1, ε_2) versus time curves and calculated biaxiallity ratios for each reference and multilayer system are given in the Supporting Information (Fig. S1). A schematic of the biaxial tensile setup is shown in Fig. 1d. XRD (Al 111 Bragg reflection, λ = 0.124 nm, spot size 300 μm, $\sin^2$psi analysis: 6 psi angles 0°-75°) and digital image correlation (DIC, on the backside of the samples) measurements were performed to measure the lattice and true strains, respectively. All samples were examined post-mortem with scanning electron microscopy (SEM, Hitachi S-4800, Japan) and FIB cross-sections.

COMSOL Multiphysics® v. 6.1. (COMSOL AB, Sweden) was used to perform simple finite element simulations on multilayers modelled according to cross-sectional TEM images. Two sinusoidal layers with 2.4 nm or 9.4 nm thickness (E = 210 GPa, wavelength = Al grain size 50 nm) were introduced in a 150 nm Al film (E_{Al} = 70 GPa). Instead of loading the multilayer with a substrate, it is

deformed at its ends along its length (x direction). 10 periods of oscillation were modelled. The structures were strained in uniaxial tension to 0.1% strain to analyze resulting strain heterogeneities as a function of interlayer thickness. Even if the mechanical description is not rigorously identical to the experiments, the aim is to describe the distribution of elastic strain induced by the sinusoidal interfaces and the strong mechanical contrast between Al and Al_2O_3.

3. Results

3.1. Structural characterization

Fig. 2 shows overview and high resolution (HR-) TEM cross-sections of the multilayer and reference films on Si substrate or Al (Fig. 2c). On polyimide, identical thin film structures were obtained, as shown in a recent publication [26]. The reference films (50 nm and 150 nm Al, Fig. 2a,b) exhibit a homogeneous film thickness. Without substrate pre-heating, the grains are not perfectly columnar. The Al sublayers in the multilayers (Fig. 2c-e) exhibit a homogenous film thickness with columnar Al grains constrained by one intermediate ALD cycle (Fig. 2c) or amorphous Al_2O_3 layers (Fig. 2 d-e), the latter clearly visible as continuous, homogeneous bands. A single ALD cycle on metal surfaces does typically not result in a continuous monolayer with full surfaces coverage [41,42], however it is enough to generate a sublayer architecture in a controlled manner, as has been demonstrated in our recent publications [16,26]. Oxide layer thicknesses were measured from corresponding HR-TEM cross-sections (Fig. 2g-h) as 3.5 ± 0.3 nm and 9.6 ± 0.2 nm. Those values are slightly higher than the calculated oxide thickness based on the GPC rate reported for Al_2O_3 under similar process conditions (0.14 nm/cycle ellipsometry measurements [66]; 17 cycles = 2.4 nm; 67 cycles = 9.4 nm). We know that accurate thickness measurements from cross-sectional TEM imaging at such small scales is limited and will lead to overestimation, as detailed in a recent publication [26] and are thus confident that no significant oxidation occurs during the PVD-ALD transfer. For further TEM analysis of amorphous ALD-Al_2O_3 layers readers are referred to Refs [16,66].

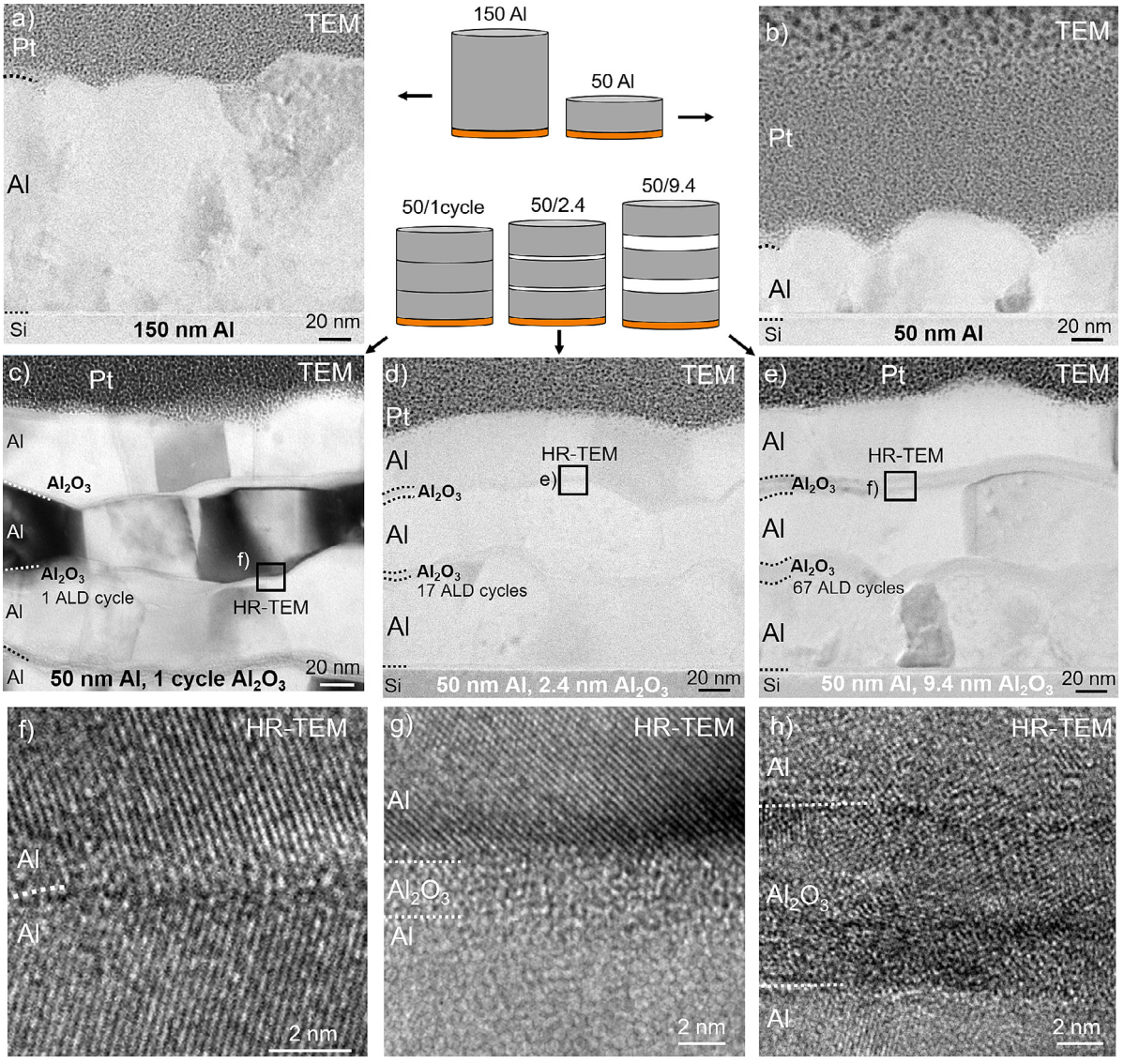

Fig. 2. TEM cross-sections of the investigated thin film systems. (a) 150 nm Al and (b) 50 nm Al reference samples. (c,d,e) Multilayers consisting of 50 nm Al sublayers with a columnar microstructure separated by 1 ALD cycle and nominally 2.4 nm and 9.4 nm thick amorphous Al_2O_3, respectively. (f-h) Corresponding HR-TEM images of two adjacent Al sublayers separated by 1 ALD cycle and amorphous Al_2O_3. The images shown in (f,g) were modified from Ref [26].

3.2. Mechanical characterization

Biaxial straining of the Al/Al_2O_3 multilayers and the Al reference samples revealed the influence of sublayer structure and oxide thickness on the mechanical behavior and crack resistance of the flexible thin film systems. Fig. 3 shows the film stress (Al 111) and full width at half maximum (FWHM, Al 111, psi 0° - or equivalently chi 90° considering chi = 90° - psi) data of Al in the different configurations during loading and unloading. The FWHM is sensitive to grain size and lattice defect density, whereby smaller grains and increasing defect densities cause peak broadening. Along with film stresses the FWHM provides important information which aids the determination of different thin film deformation regimes [50]. All FWHM curves recorded at different chi angles are reported in the supporting information (Fig. S2). For the multilayers, the measured signal is an average of the three Al sublayers, since the method is unable to resolve individual layers of the same material in film thickness direction. Due to the amorphous nature and small thickness of the Al_2O_3, no XRD signal could be obtained from these layers.

Comparison of the two reference samples (Fig. 3a,b) shows that smaller grains in the 50 nm Al film cause generally increased initial FWHM values as compared to 150 nm Al, because the size of diffraction coherent domains is lower. Identical initial slopes of the film stress curves indicate a constant Young's modulus independent of the film thickness ($E \sim 77$ GPa), which is close to Al bulk

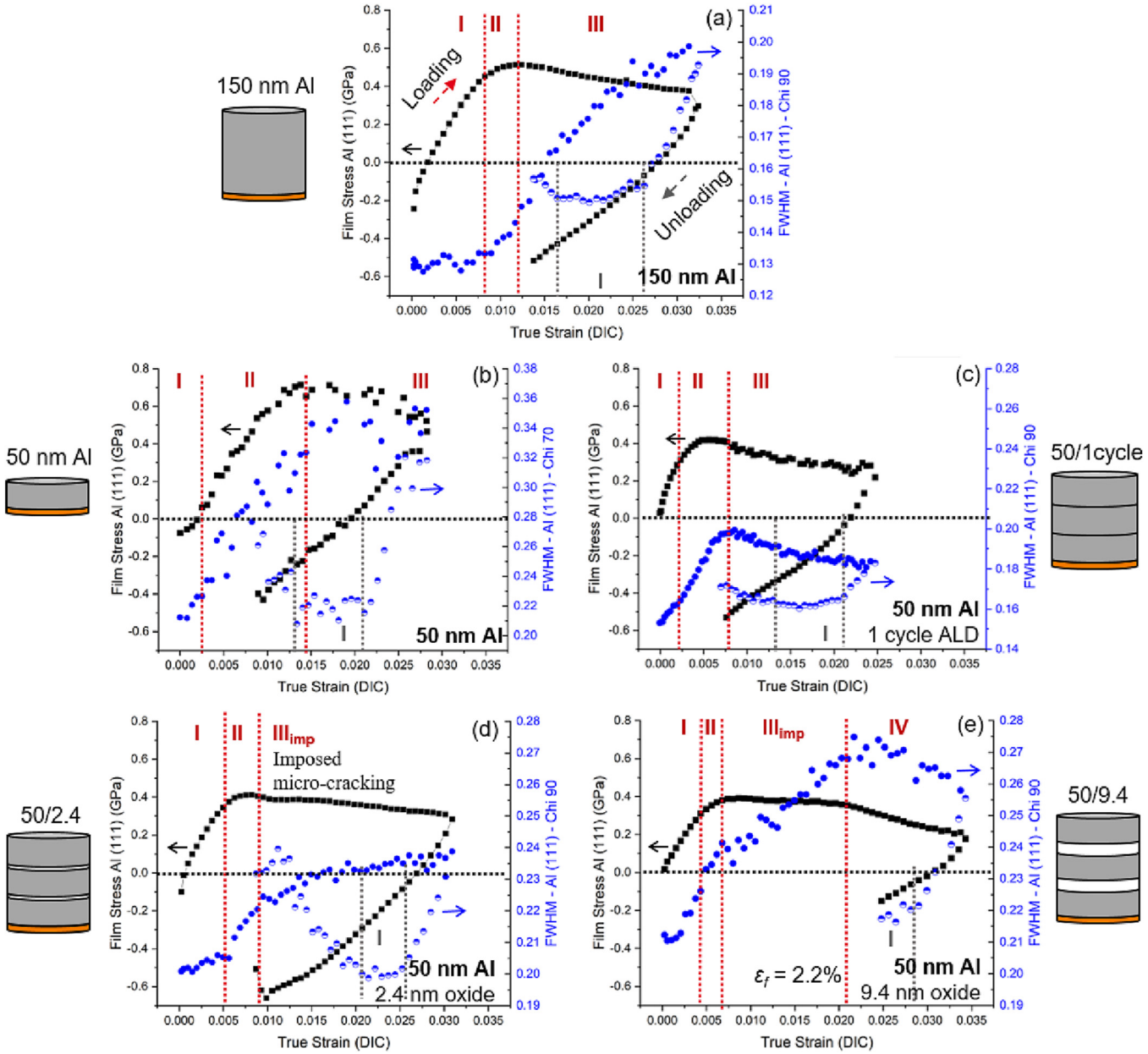

Fig. 3. Al film stress and FWHM (Al 111 peak) as a function of applied strain (loading & unloading) measured from *in situ* XRD biaxial straining experiments. Depending on the Al sublayer structure and oxide thickness different deformation domains are observed during loading, indicated by red dashed lines. (I: Elastic, II: Micro-plastic, III: Necking, III_{imp}: Imposed micro-cracking, IV: Fragmentation). (a) 150 nm Al reference, exhibiting typical ductile thin film deformation. (b) 50 nm Al reference, showing ductile deformation with increased scatter in the data due to a weaker XRD signal. The reader should note the differing scale for FWHM in this case. (c) Multilayer of 50 nm Al sublayers separated by 1 cycle Al_2O_3. The increased scatter in regime III is an experimental artefact. (d) Multilayer of 50 nm Al sublayers with 2.4 nm Al_2O_3 showing micro-cracking. (e) Multilayer of 50 nm Al sublayers with 9.4 nm Al_2O_3 showing micro-cracking and fragmentation at 2.2% strain. (For interpretation of the references to colour in this figure legend, the reader is referred to the web version of this article.)

counterparts. As expected, the thinner Al film exhibits a higher maximum stress, σ_{max}. It is important to note that the weak XRD signal of the 50 nm Al film is responsible for the larger scatter of the stress and particularly the FWHM curve as compared to thicker Al and multilayers. Peak fitting for the 50 nm film was only possible for a reduced number of psi angles, resulting in a slight overestimation of the maximum stress for 50 nm Al film, as analysis of the 150 nm Al data with reduced psi angles shows an increase in the maximum stress (510 MPa – 6 psi angles; 590 MPa – 3 psi angles). Nevertheless, the difference between σ_{max} for 50 nm and 150 nm Al remains significant.

Starting with the 150 nm pure Al reference sample, 3 different domains can be distinguished during loading based on the evolution of stress and FWHM as a function of applied strain (Fig. 3a). Domain I is characterized by a linear increase of the stress–strain curve and a constant value of the FWHM and equals elastic deformation. In Domain II a bending over of the stress–strain curve and a simultaneous increase in FWHM are observed, related to microplasticity and the onset of dislocation activity. In Domain III, the final region within the applied strain regime, the film stress slowly decreases, while FWHM continues to increase with a different slope compared to Domain II. This domain corresponds to localized plastic deformation (necking), characteristic for ductile thin films on polymers [32,67]. Similar regions have been previously identified for biaxially strained ductile flexible thin films [50,52]. Depending on the film thickness, the stress in Domain III exhibits different trends. For 50 nm Ni thin films [50] a stress decrease similar to 150 nm Al is observed, whereby this stress decrease in Ni is due to brittle multi-cracking. Thicker films (250 nm Al [52]) can exhibit a pronounced stress plateau in the beginning of Domain III. In uniaxial tensile experiments, Gruber et al. [36] found a stress plateau for Cu thin films (30–1000 nm), governed by very homogeneous size-dependent dislocation plasticity, to which each grain has to contribute [36,68]. Only for the thinnest Cu films (<50 nm), grain boundary sliding may become an additional deformation mechanism, when dislocation plasticity is increasingly constrained and inhomogeneous elastic lattice strains between individual grains have to be accommodated in the grain boundary network [68,69]. Upon further straining Domain III typically progresses to fragmentation or through-thickness cracking, resulting in pronounced stress relaxation and a constant plateau of the FWHM [52]. Within the applied strain regime, the 150 nm Al film does not exhibit fragmentation in the stress or FWHM data. In contrast, the onset of biaxial fragmentation in 250 nm Al is observed around 2% applied strain [52].

In the beginning of unloading, a decrease in film stress and a rapid decrease of FWHM are observed, potentially due to closure of tensile induced defects. Around zero film stress, another elastic deformation regime is observed (Domain I, Fig. 3a), characterized, equivalently to loading, by constant FWHM and a linear increase of compressive stresses, as a result of continued elastic relaxation of the polymer substrate. The plateau value of FWHM is higher as compared to the initial FWHM, potentially indicating an increased lattice defect density and dislocation storage. The reduced slope of the accumulating compressive film stress compared to initial loading, can be explained by tensile induced defects resulting in a less dense material. Finally, another increase in FWHM is observed, indicating increasing dislocation activity as a result of the accumulated compressive stresses.

Fig. 3b shows the stress and FWHM (chi 70° - due to reduced data fit possibility mentioned earlier) response of the thinner 50 nm Al reference sample. Scatter of the data due to the weak XRD signal, especially for the FWHM curve, makes it difficult to identify and interpret individual deformation regimes in detail. Furthermore, the different chi angle slightly influences the FWHM evolution (see supporting information (Fig. S2)). For the thicker films with stronger XRD signal lower chi angles typically cause slightly increased initial values and a more plateau like behavior in Domain III compared to chi 90. In contrast to 150 nm Al, the FWHM plateau in the beginning (Domain I, elastic deformation) appears to be extremely short and an almost immediate increase of FWHM upon straining is observed for the thinner Al film, indicating an increasing number of lattice defects while the film stress increases linearly. Compared to all other samples, the 50 nm Al film shows the highest relative FWHM increase within the applied strain range. After the maximum film stress is reached, a more plateau-like progression of FWHM is suggested. The unloading behavior is similar as previously discussed for 150 nm Al with the difference that FWHM during unloading recovers down to initial FWHM values before the final increase. This is in alignment with the difficulty of storing dislocations in very thin films (<100 nm) [70]. For grain sizes or film thicknesses below 100 nm, also the nucleation stress for a partial dislocation becomes lower than the activation stress for a full dislocation source [71].

Al sublayer structure and oxide layer thickness strongly influence the deformation behavior. Fig. 3c shows the stress and FWHM response of Al sublayers separated by a single cycle of ALD-Al_2O_3. Initial FWHM values lie between the 50 nm and 150 nm Al reference films. This is likely due to a slightly larger in-plane grain size (91 ± 27 nm) compared to the other multilayer samples. The length of Domain I is comparable to the 50 nm Al reference. The typical transition from constant to increasing FWHM at the beginning of Domain II is more pronounced at lower chi angles (see Supporting Information, Fig. S2). The maximum stress (418 MPa) is lower compared to the single 150 nm Al layer despite the reduced grain size in the sublayers. Domain III is characterized by a gradual decrease of stress and, in contrast to the reference films, decreasing FWHM, which could be a signature of hole formation (Section 3.3). The increased scatter in the data in this regime is an experimental artefact due to slipping of the sample in the grippers and not a signature of thin film deformation and the maximum applied strain is slightly lower compared to the tested sample series. During unloading, FWHM recovers to almost initial values.

Fig. 3d-e show the stress and FWHM response of the Al/Al_2O_3 multilayers with 2.4 nm and 9.4 nm Al_2O_3 layers, respectively. In the comparison between these two conditions the FWHM is a particularly valuable indicator as domain size, texture and diffracting volume are maintained constant, such that the only differential contribution to FWHM remaining must be microstrain, or dislocation density. In all cases, initial FWHM values are comparable to the 50 nm Al reference and slightly higher than for the 50/1cycle sample. For the 50/2.4 sample (Fig. 3d) purely elastic behavior similar to 150 nm Al (Domain I: linear stress increase, constant FWHM) is observed up to a strain of 0.006. The maximum stress (412 MPa) is lower compared to the single Al layers and 50/1cycle. The elastic domain is followed by a short region of micro plasticity (Domain II) with increasing FWHM and a bending over of the stress curve. Subsequently, a stress plateau and slow decrease of the film stress are observed. In contrast to the 150 nm Al reference (Domain III, necking, increasing FWHM) and the 50/1cycle film (decreasing FWHM), FWHM in this Domain $III_{imp.}$ is slowly approaching a plateau value, indicating reduced plasticity and dislocation activity in Al and potentially micro-cracking imposed by the oxide layers. Short and scattered through-thickness cracks have been observed post-mortem. For biaxially strained Al/Mo (250–75 nm/50 nm) bilayers, Cordill et al. [52,72] show that moderate stress relaxation with a constant (250 nm Al) or moderately increasing FWHM (75–125 nm Al) corresponds to reduced plasticity in the ductile layer due to the presence of Mo, depending on the bilayer architecture. The fact that no clear FWHM plateau is reached in our case is likely due to the reduced metal layer thickness. The unloading behavior is similar to the 50 nm Al reference sample, with complete recov-

ery of FWHM and elastic deformation (constant FWHM, linear compressive stress increase) followed by plasticity as a result of compressive stresses (pronounced FWHM increase, change of stress–strain slope).

Increasing the oxide layer thickness in the multilayer further changes the mechanical behavior of the Al sublayers. With 9.4 nm Al_2O_3 (Fig. 3e) the pure elastic regime (Domain I, linear stress increase) shows an increase of FWHM; later, we attribute this to strain heterogeneities from wavy interfaces and high Young's modulus contrast (see Section 4.2). The maximum stress (392 MPa) is slightly lower as compared to the multilayer with 2.4 nm oxide layers. Domain $III_{imp.}$ is similar to 50/2.4 with a slightly decreasing almost constant film stress and increasing FWHM. The steeper slope of FWHM in Domain $III_{imp.}$ could be the signature of individual sublayer fracture and a higher density of microcracks on one sublayer. Inhomogeneous crack distribution in the film thickness direction should lead to higher FWHM values as compared to homogeneously distributed defects. Sublayer fracture with adjacent layers remaining intact has been observed during the post-mortem cross-sectional analysis in this work (see next section) and in our recently published uniaxial tensile study [26]. Instead of a plateau, sudden drops in FWHM and film stress are observed around 2.2% strain, corresponding to fragmentation or through-thickness cracking of a subset or all Al sublayers. Through-thickness cracking locally relaxes the stress along the crack edges, leading to a pronounced decrease in the average stress measured in the film. The 50/9.4 sample is the only film system clearly exhibiting fragmentation in the stress data within the applied strain range. For Mo/Al/polyimide systems [52], Al fragmentation exhibits a comparable stress decrease but constant FWHM values. The Mo layer on the other hand fragments with a decrease in stress and FWHM, similar to Al in the 50/9.4 sample. Differences in the FWHM behavior during fragmentation are potentially due to the layer order and the Al sublayer structure and are not well understood at the moment. The initial unloading behavior of 50/9.4 is similar to 50/2.4, with differences in the extent of the FWHM recovery, which does not seem to reach all the way down to initial values. In the subsequent elastic unloading regime, the slope of the stress strain curve is significantly lower compared to all other samples, as a result of fragmentation and a higher crack density. Unfortunately, the second half of the unloading segment was not recorded due to experimental issues. The buildup of compressive stresses upon unloading has been previously observed for uniaxially strained thin films on polymer substrates [26,59] whereby fractured films exhibit lower compressive stresses after unloading compared to plastically deforming, ductile ones.

3.3. Post-Mortem SEM and FIB characterization

Post straining characterization with SEM (Fig. 4a-e) shows the lateral deformation/fragmentation damage of the multilayers and Al references. Tensile axes are indicated with white arrows. Generally, the surface roughness of the thicker 150 nm Al layer is higher as compared to the 50 nm Al single layer and the ALD/PVD multilayers. The circular white features visible in the inset in Fig. 4a are likely hillocks, small outgrowths on the film surface, forming as a result of compressive residual stresses [73-75], which are indeed present in the 150 nm Al film (Fig. 3a) at a higher magnitude compared to all other film systems (Fig. 3b-e).

For the two Al reference samples and the 50/1cycle multilayer (Fig. 4a-c) no pronounced crack pattern is visible on the surface, as suggested by the film stress data. Only faint traces of 2D tensile induced deformation (necks, which could transform into through-thickness cracks) can be found in the overview image of the 150 nm Al sample. Vertical lines in Fig. 4a are surface scratches

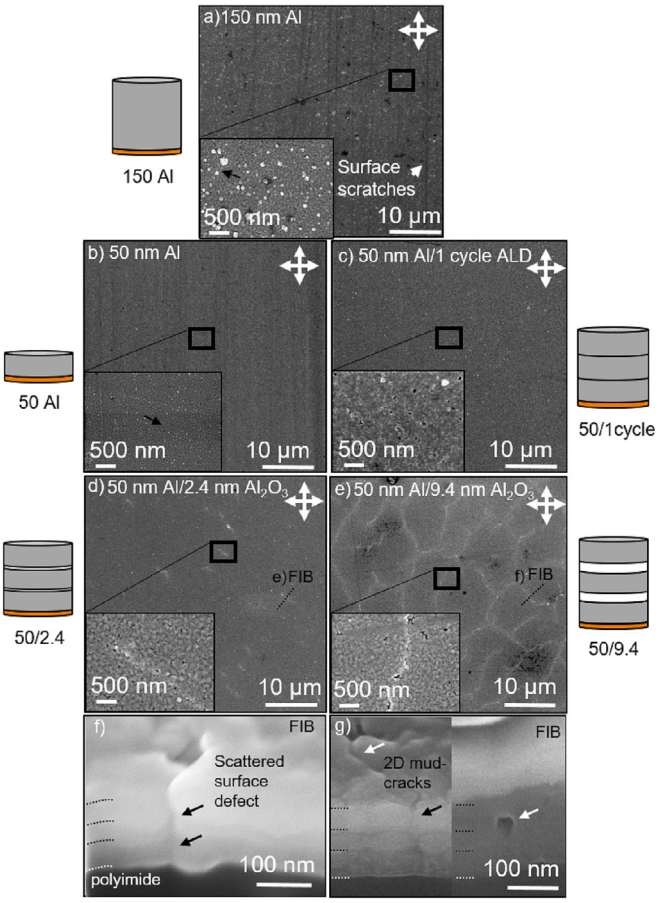

Fig. 4. Post-mortem SEM/FIB characterization of the samples after equibiaxial loading. Only faint traces of 2D tensile induced deformation are visible in (a) the overview image of the 150 nm Al sample, whereas the surface of the 50 nm film (b) appears defect free. Vertical lines in (a) are scratches due to handling. At higher magnification (insets a-b) small crack-like defects can be found for both samples, indicated by black arrows. (c) 50/1cycle sample showing no cracks but small local defects at grain boundaries and triple points at high magnifications (inset), which are also present in the other multilayer films. (d) Scattered surface defects are visible for multilayers of 50 nm Al and 2.4 nm Al_2O_3. (e) A pronounced 2D mud-crack pattern is visible for multilayers of 50 nm Al and 9.4 nm Al_2O_3. (f,g) Corresponding FIB cross-sections showing tensile induced defects penetrating all Al sublayers (f, g – left image) or internal fracture of individual Al sublayers (g - right image). Al sublayers and defects are indicated with dashed lines and arrows, respectively. The representative positions of the FIB cuts are indicated in d) and e).

due to sample handling. The surface of the thinner 50 nm film appears defect free at low magnifications. Please note that the thinner Al film and the 50/1cycle sample have been strained to a slightly lower maximum value. At higher magnification (insets) small crack-like defects can be found for both pure Al films (black arrows). Local early stage necking of ductile thin films is difficult to observe, especially with elastic recovery of the polymer substrate after unloading [33]. *In situ* experiments with high-resolution quantitative surface analysis methods such as atomic force microscopy are typically used to carefully trace deformation in such material systems [32]. Post-mortem cross-sectional analysis of biaxially strained ductile Al thin films (250 nm) can be found in Ref. [52]. The absence of a 2D deformation pattern at low magnifications for the 50 nm Al film could indicate grain boundary sliding as an additional deformation mechanism as suggested for < 50 nm Cu films in Ref. [36,68,69]. The Cu study in Ref. [36] however, does not include a post mortem SEM analysis of the sample surface for direct comparison.

On the contrary, a pronounced 2D mud-crack pattern, typical for equibiaxial loading [50,76], is observed in the multilayer with

9.4 nm oxides (Fig. 4e). Cracks in Al are in agreement with the relaxation of Al film stresses observed at ε_f = 2.2%. The 50/2.4 sample (Fig. 4d) however, only exhibits scattered surface defects. Correspondingly, no pronounced stress relaxation was observed in the XRD data. Both 2D cracks and scattered defects appear to be closed, with contacting crack edges, as a results of polymer relaxation after unloading. The scattered surface defects in Fig. 4d seem to have one preferential orientation approximately 45° inclined to the pulling axes. Similar crack orientations can be found in the 2D crack pattern in Fig. 4e. The reason for a dominant orientation of scattered surface defects is not fully understood. One explanation could be a weakest link type of phenomenon caused by the specific microstructure of the Al sublayers (co-deposition from two targets without substrate rotation). Another influencing factor could be the direction of the maximum in-plane normal stress during quasi-equibiaxial loading, facilitating cracking perpendicular to that direction. For biaxially loaded brittle Cr thin films (100 nm thickness) a small deviation from the equibiaxial condition (loading ratio x:y = 1:1.1) can lead to a preferential orientation of the first cracks, which evens out during progressive fragmentation [53].

The most prominent features on the surface of the 50/1 cycle sample after straining are small holes at grain boundaries, visible as black spots in the inset in Fig. 4c. These defects appear to be a local, tension-induced opening of grain boundaries or triple points, but do not initiate extensive cracking. They are only found in the highly strained center of the tensile specimen, also for the other multilayer samples (insets Fig. 4 d-e). Single Al films do not exhibit this type of grain boundary defects, indicating that it is related to the sublayer architecture.

FIB cross-sections reveal the film damage in the thickness direction. Cross-sectional analysis is exacerbated by the low film thickness, charging effects from the polymer substrate and crack closure due to polymer relaxation. Still, the Al sublayer structure can be resolved in most cases. Representative cross-sections of a scattered surface defect and 2D cracks are shown in Fig. 4f-g. In both cases, some form of structural defect appears to penetrate all three Al sublayers. However, there is also evidence that at low strains only individual Al sublayers fracture, while adjacent Al layers remain intact. Fig. 4g also shows fracture of only the middle Al sublayer. The small defect at the Al-polyimide interface can be due to straining or damage from the electron beam during imaging. Prior to cutting, a protective Pt layer was applied in this case. Cracking of the middle Al sublayer was identified while cross-sectioning a discontinuous crack visible on the surface in an area where the surface was still intact. With increasing applied strain, individual sublayer cracks will likely transform into through-thickness cracks. Statistical analysis of cross-sectional crack propagation is difficult due to exacerbated imaging. From a total number of 12 cracks cross-sectioned for the 50/9.4 sample, 2 cross-sections clearly identified individual sublayer fracture and 6 confirm through-thickness failure. The remaining four cuts did not yield a clear result. Finite element modelling of the polymer substrate under biaxial loading shows that there is only elastic and no plastic deformation in the center of the crucible within the applied strain range [72]. Cracks should therefore be able to close completely upon unloading such that a healing mechanism as in nanoindentation of Al/TiN [77] may be possible. Only at higher applied strains would cracks be maintained open in the unloaded state by the permanently deformed polymer substrate thereby geometrically prohibiting such healing mechanisms.

4. Discussion

4.1. Deformation of the metal layer

Typically, thin film strengthening is observed as a function of decreasing layer thickness within the present thickness range for series of single layers [37] and multilayers [29,37]. The maximum stress, σ_{max}, and 0.2% yield stress values of the Al sublayers in the different configurations, derived from the *in situ* film stress measurements, are summarized in Table 1. The two values are identical for the 50 nm Al films and very close to one other in all other cases. While the single 50 nm and 150 nm Al reference samples follow the common strengthening trend, the 50 nm Al sublayers in the 50/1cycle sample and Al/Al_2O_3 multilayers exhibit progressively lower maximum stresses in biaxial tension with introduction and increasing of the oxide thickness and their maximum stress and the end of Domain II (microplasticity) are shifted to lower applied strains (Table 1). However, direct comparison of strengths between references and multilayer films is complicated by unavoidable changes in either grain size (150 nm Al) or total film thickness (50 nm Al). Rather than being a benchmark in terms of strength, the 50 nm and 150 nm Al reference sample here serve as model systems for ductile thin film deformation. In fact, it is known that for ductile thin films on polymer substrates, bilayers including brittle components can perform somewhat worse than their equal-thickness single layer counterparts (75–200 nm Al with 50 nm Mo on PI, biaxial [52,72]; 50–200 nm Cu with 10 nm Cr on PI, uniaxial [37]).

On the contrary, there are many examples in literature under similar loading conditions, involving works on Al and Cu thin films, which capture extra hardening in multilayers associated to the presence of penetrable versus impenetrable grain boundaries, or with respect to the presence of a free surface or an impenetrable cap layer. All top layers in the multilayers as well as the 50 nm single Al film have a natural oxide capping layer of roughly 5 nm as a result of exposure to ambient air. Additionally, the ALD-Al_2O_3 interlayers act as impenetrable barriers on the top and bottom of each Al grain in the sublayers. Compared to the natural oxide, these interlayers are thinner (2.4 nm) and thicker (9.4 nm) depending on the specific sample. Gruber et al. [36] found that Cu films (20–100 nm) confined by Ta layers (10 nm) on one or both sides exhibit a large increase in flow stress compared to single Cu layers; the difference between one or two capped sides being very small. Similarly, work by de Boer et al. [78] shows a change in strength of ~200 nm free-standing Al films capped on both sides by an oxide layer, which constrain dislocation glide. The reason we do not perceive impenetrable layer strengthening in our Al sublayers in biaxial tension may be related to stress concentration due to the internal roughness and stiffness contrast of the multilayers (Section 4.2) or deformation/fracture of the ALD-oxide layers before yielding of Al, similar to cracking induced by adhesion layers [37]. Certainly, this only applies to ALD-Al_2O_3 layers within the multilayers, since no fracture is observed for the pure 50 nm Al film, also suggesting that free surface may be useful for the plasticity of oxide layers. However, clear fracture of Al_2O_3 is only observed for 9.4 nm thickness. Factors that potentially contribute to weakening of the internal oxide layers are detailed in Section 4.2.

It appears that the presence of oxide layers is not always prohibiting strengthening, since in polymer-supported uniaxial tensile tests of similar multilayers, an increase of σ_{max} has been observed for Al sublayers with increasing oxide thickness [26], indicating that the weakening of Al reported here is related to the biaxial loading condition. The stress values measured parallel to the loading direction, recently published in a related work [26], are included in Table 1 for comparison. It should be noted that the low strain rates of uniaxial (8×10^{-5}/s) and equibiaxial (7×10^{-6}/s) tests differ by one order of magnitude. Sub-μm Al single crystals show a noticeable strain rate dependence in the regime of 10^{-3}/s to 10^{-4}/s [79]. Free-standing amorphous Al_2O_3 films [80] also exhibit a strain-rate dependence of strength and ductility. The strain rate sensitivity of free-standing nanocrystalline Al films with a similar

Table 1
Mechanical properties of Al sublayers in different multilayer configurations, derived from *in situ* film stress measurements. The maximum stress, σ_{max}, and 0.2% yield stress (in brackets) during biaxial testing are reported along with the applied strain at maximum stress, ε. For further calculations, stress values from quasi-uniaxial polymer-supported tensile tests [26] are included. Using the von Mises yield criterion, the uniaxial tensile stress of Al, σ_x, of Al in the different layer architectures can be predicted.

Configuration Al-Al_2O_3 [nm]	50	150	50/1cycle	50/2.4	50/9.4
σ_{max} Al [MPa] quasi-equibiaxial (7×10^{-6}/s)	715 (715)	513 (492)	418 (410)	412 (408)	392 (386)
ε @ σ_{max} [%]	1.4	1.2	0.5	0.8	0.9
σ_{max} Al [MPa] quasi-uniaxial (8×10^{-5}/s) [a]	~560	305	360	504	516
σ_x Al uniaxial [MPa], predicted using von Mises yield criterion	360	171	282	500	(569)[b]

[a]Values included from Ref [26] for comparison.
[b]Von Mises yield criterion not valid.

grain size (~62 nm) to the present has previously been determined at room temperature to be 0.037 [81]. This would imply only a 9% yield stress increase from 10^{-6} to 10^{-5}/s which may be considered as a worst case as stress coupled grain growth in nanocrystalline Al, which normally serves to increase strain rate sensitivity [81], is expected to be suppressed in the film normal direction here by the oxide interlayers.

Regarding different loading ratios, thin metal films on polymer substrates (50 nm Ni [50]) are stronger in equibiaxial tension compared to uniaxial tensile loading, in line with the results obtained for the 50 nm Al and 150 nm Al reference films (Table 1). For ceramics on the other hand, the fracture strength can decrease with increasing multiaxiality of loading, such that crystalline alumina exhibits a strength decrease of 8.5% in equibiaxial tension compared to the uniaxial case [82], while for thin amorphous SiO_x coatings on polymer substrates a biaxial strength value (260 MPa) close to the uniaxial case (280 MPa) was found [47,48]. It is, therefore, suggested that the observed weakening of the Al layers in the multilayers under biaxial loading, which exhibit strengthening in uniaxial tension, results from a biaxial weakening of Al_2O_3 in the multilayers, whose deformation behavior dominates.

The unloading portion of the tensile tests also contains important information about Al deformation and tensile induced defect density. Of particular interest are the FWHM recovery and the slope of the film stress in the elastic film regime during unloading. It is expected based on literature [71] that 150 nm Al films are favorable for full dislocation storage, while 50 nm Al films are more favorable for partial dislocation nucleation and absorption at grain boundaries, which can be characterized by recovery of the FWHM during unloading. Importantly, the pertinent parameter is not only film thickness but also the lateral grain size (97 ± 31 nm and 42 ± 14 nm, for 150 nm and 50 nm films, respectively [26]). After a rapid initial decrease of FWHM upon unloading, we observe complete or almost complete reversibility of FWHM for all 50 nm Al films (reference plus sublayers), but not for 150 nm Al. This reversibility could be the signature of dislocation storage, indicating that in the 50 nm layers the grain size is too small to store any dislocation disappearing into the grain boundaries. In the same way, it is proof of plasticity through a dislocation mechanism in the case of 150 nm Al. Initial impingement of dislocation and disappearance of such during further straining has been observed at the crystalline/amorphous Al/PI interface [83]. The multilayers contain further crystalline/amorphous Al/Al_2O_3 interfaces, which could potentially act in a similar way – pinning of dislocation arms at such interfaces being previously suggested by post-mortem observation of microcompression pillars [16]. Regarding the film stress evolution in the elastic unloading regime, compressive stresses, resulting from continued elastic relaxation of the polymer, develop with a reduced slope as compared to initial elastic tensile loading for all film systems. This can be explained by tensile induced defects (necks and cracks), reducing the density of the material and, similar to porosity, causing a lower apparent Young's modulus. A similar slope, determined from the first five points of the unloading segment in Fig. 2, for the reference samples (150 nm Al: 63 GPa, 50 nm Al: 48 GPa) and the samples with 1 cycle ALD (60 GPa) and 2.4 nm oxides (58 GPa), indicates low densities of tensile induced defects, while a significantly reduced slope with 9.4 nm oxides (31 GPa) correlates to more extensive cracking, as confirmed by the post-mortem SEM analysis. Differences in the defect density between 50 nm and 150 nm Al are expected due to the known film thickness dependence of the crack spacing [84].

4.2. Deformation of the oxide layers

While deformation of the oxide layers cannot be traced directly with the presented XRD and post-mortem SEM/FIB approach, some indirect conclusions about oxide deformation can be drawn based on the deformation of the Al sublayers. For the 50/2.4 and 50/9.4 sample, the only structural difference is the thickness of the oxide layers, since both multilayers exhibit a similar in-plane grain size of 54 ± 20 nm (50/2.4) and 42 ± 18 nm (50/9.4) [26]. Here, the FWHM is a particularly valuable indicator, as domain size, texture and diffracting volume of Al are maintained constant, such that the only differential contribution to FWHM remaining must be microstrain or dislocation density. Fig. 5a shows the loading portions of the FWHM curves of the 50/2.4 and 50/9.4 sample, normalized to their respective initial values $FWHM_0$, along with the film stress data to better visualize the boundaries of deformation domains. Differences are observed in the FWHM evolution, especially before yielding of the Al layers, indicating that with thicker oxides more is happening (FWHM increase at the beginning of hashed yellow region), while with thinner oxides, the first abrupt increase in FWHM correlates well with yielding of the metal layers (end of hashed yellow region). A further change in slope of FWHM around the onset of metal yielding is also visible with 9.4 nm oxides.

Since both multilayers have the same number/area of interfaces, interface driven processes such as dislocation nucleation/sinks should not change. Finite element simulations of our structures, modelled according to the cross-sectional TEM analysis (Fig. 2d-e), show that the observed differences in the early FWHM behavior are likely due to elastic strain heterogeneities, resulting from the internal waviness of the multilayer architecture combined with the stiffness contrast between Al and Al_2O_3 (factor 3) and higher rigidity of the thicker oxides. It is shown in Fig. 5b-c that for sinusoidal Al_2O_3 interlayers (wavelength 50 nm = Al grain size), the magnitude of the strain heterogeneity created in the Al sublayers in the z direction (ε_{zz}) at 0.1% applied strain horizontally is about 3.5 higher when increasing the oxide thickness from 2.4 to 9.4 nm. Indeed, the standard deviation for ε_{zz} in the simulations is 1.2×10^{-5} and 4.2×10^{-5}, respectively, and is directly related to FWHM along the scattering vector (measured here along the z-direction) in an *in situ* XRD experiment (especially in the elastic domain). If we plot the relative FWHM evolution as a function of strain, we find an about 5 times higher ratio at the yield point

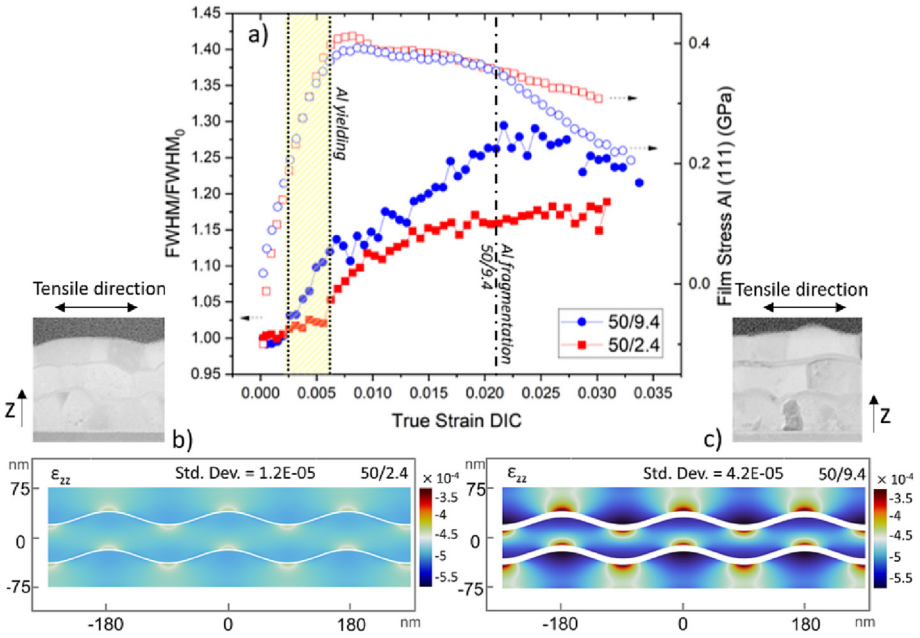

Fig. 5. Multilayer deformation as a function of oxide thickness. a) Film stress (open symbols) and normalized evolution of the peak width (FWHM, Al 111, filled symbols) with 2.4 nm and 9.4 nm oxides during biaxial tensile loading, highlighting a different FWHM behavior before yielding of Al (yellow region). b-c) Finite element simulations of multilayers with wavy 2.4 nm (b) and 9.4 nm (c) oxide layers, showing the increased magnitude of strain heterogeneity in the cross-section in the ε_{zz} direction with thicker interlayers at 0.1% applied strain. Tensile direction is indicated with black arrows. Cross-sections were modelled according to TEM analysis of the real structures. (For interpretation of the references to colour in this figure legend, the reader is referred to the web version of this article.)

for the 50/9.4 sample as compared to 50/2.4. The simulated waviness is more regular and therefore less severe compared to the real case, causing locally higher heterogeneities which could explain the difference between simulation results and experimental observations. It should be noted here that if the interfaces were planar instead, there is no intra-layer ε_{zz} heterogeneity, e.g. heterogeneity inside the Al layer, only ε_{zz} contrast between Al_2O_3 and Al. The increased elastic heterogeneities are possibly also the cause of the observed earlier yielding at lower applied strains. Adjustment of sputter parameters (working pressure, temperature [85]) can reduce roughness of thin Al layers for more homogeneous multilayers and reduced stress localization, which can act as initiation for local necking/micro-cracking of Al.

Certainly fragmentation of Al sublayers in Domain IV, as confirmed by the pronounced 2D crack pattern on the surface, suggests that the thicker oxides fracture locally at relatively low applied strains. Previously, stress concentration at fracture sites of brittle films in multilayers [37,59] has been related to early fragmentation and pronounced through-thickness cracking of ductile layers, similar to the 50/9.4 sample, with other *in situ* XRD experiments [37,59,60,86]. It has been shown in brittle-ductile bi and tri-layer systems that, depending on the total film thickness, thickness ratio and position of the brittle layers, fragmentation can happen concurrently in both layers or consecutively in a two-stage manner [52,86,87]. In our multilayers, the thickness ratio is such that both cases have been reported, the relative position of Al_2O_3 and Al depends on the sublayer under consideration and the recorded stress data is an average value, not resolving individual Al sublayers. Therefore, fracture of the 9.4 nm oxides could happen concurrently at 2.2% or at lower applied strain values. When the oxide thickness is reduced down to 2.4 nm, no early FWHM increase or sudden, pronounced stress decrease (Domain IV) are observed and only scattered surface defects are visible after straining. Two scenarios are plausible to explain this improved cracking resistance, whereby the experimental data cannot determine with certainty which one is the case: Either (i) the thinner oxides do not fracture substantially within the applied strain range due to structural perfection and low defect density, causing only a small number of scattered defects or (ii) fracture occurs but the stress concentration at the fracture sites is not high enough to cause substantial fragmentation of adjacent Al sublayers.

Literature has shown, that provided a perfect structure and the absence of geometrical defects, ultrathin amorphous Al_2O_3 layers can be extremely strong and ductile, whereby the limiting factor for structural perfection is often oxide layer thickness. Micro pillar compression experiments of similar Al/Al_2O_3 multilayers to 15% compressive strain [16], where the in-plane biaxial tensile strain can reach up to 10.5%, identified the limiting thickness for cracking of oxide layers above or equal to 5 nm. This thickness limit is in line with the differences observed between 2.4 nm and 9.4 nm oxide thickness in the current biaxial and a previous uniaxial [26] study. Even free-standing 40 nm thick amorphous Al_2O_3 films produced by pulsed layer deposition can deform up to 15% strain in tension without fracture at room temperature and high strain rate by a viscous creep mechanism [25]. For a thorough discussion on the impact of deposition method and purity on oxide deformation readers are referred to [26]. For polymer supported multilayer systems, Cordill et al. [52] recently showed that the position of the brittle component determines its fracture behaviour. In Al/Mo bilayer systems, highest Mo fracture strains and stresses were achieved when the Mo is directly interfacing the polymer substrate, while a reversed order resulted in fracture at considerably lower film stresses and applied strains, as a result of strain heterogeneities. Geandier et al. [88] predicted that large grain anisotropy in biaxially loaded ductile layers (Cu-like) can generate strong intergranular interactions and a large heterogeneity in the in-plane stress distribution. As a result, stress heterogeneity is induced in adjacent, mechanically isotropic W layers through interaction with Cu grains that deform heterogeneously. In the present case, strain heterogeneities in the Al layers in Domain I and II are revealed by FWHM and simulations. By displacement continuity at the interfaces, these heterogeneities are at least partially

transmitted to the oxide layers. This strain localization is potentially a factor of cracking.

4.3. Lateral and through-thickness crack resistance

The observation of small intergranular holes on the surface of the multilayers after biaxial loading (insets Fig. 4c-e) is specific to this study and not among the commonly reported deformation mechanisms (necking, cracking) of flexible thin films. Direct comparison to the single Al films deformed under identical conditions indicates a clear connection to the sublayer architecture. Additionally, the loading ratio seems to play a role here, since no such features are observed after uniaxial tensile loading of similar multilayer structures [26]. While this is a clear example of the importance of studying different loading ratios for thin films with complex microstructure, the total impact of this specific failure mechanism on the overall crack resistance of our films is minor, as no extensive cracking is triggered by the local defects.

In addition to the reduced lateral surface damage with decreasing oxide thickness, there is evidence in the FWHM data and post-mortem cross-sectional imaging that individual sublayers fracture before complete through-thickness failure is observed with increasing applied strain. The fact that even for the 50/9.4 sample, showing a fully developed 2D pattern on the surface, the film stress (Fig. 3e) has not fully relaxed to plateau levels comparable with literature [37,59] further supports the assumption of individual sublayer fragmentation. In uniaxial tension [26], isolated sub-layer fracture was observed in such multilayers even up to a total applied strain of 12%, with the middle Al layer preferably remaining intact. This indicates that the loading ratio might influence sublayer crack initiation and propagation: only the middle Al layer is failing in Fig. 4g, which was never observed in the uniaxial case, even though statistical analysis is difficult due to exacerbated imaging conditions. Hwang et al. [24,89] showed sublayer cracking and crack deflection in Cu/graphene multilayers as a results of cyclic bending. Al sublayer fracture with adjacent Al layers remaining intact would have a very positive effect on the damage tolerance, as individual sublayers remain connected for electron flow potentially maintaining a low electrical resistance. We expect the oxide layers up to 2.4 nm to be reasonably conductive. For Al-Al_2O_3-Al junctions, the Simmons barrier width at room temperature has been determined to lie in the range 2.08–2.9 nm [90,91], whereby the structural details of the Al/Al_2O_3 interface influence the formation of the tunnel barrier profiles [92]. Further work specific to ALD layers on PVD-deposited metal electrodes has investigated the effect of local non-planarities on the barrier properties measured [93]. Note that ALD layers there were produced using O_2 plasma instead of H_2O, avoiding the problem of H contamination, which, using our process, can be controlled via the ALD deposition temperature and microwave plasma generators for H_2O [94,95]. This constitutes a major step towards engineering the robustness of the current path in flexible electro materials and improving the tolerance for cracking: electrons can tunnel through thin oxide layers to circumvent a crack if a single sublayer fracture interrupts the current path.

4.4. Model for biaxial yield surface

To fully describe the stress state experienced by the multilayers during quasi-equibiaxial loading, the stress component σ_y, orthogonal to the experimentally determined 0.2% yield stress component, σ_x, was calculated, using the following equation:

$$\sigma_y = \frac{(1 + c * \nu)}{c + \nu} * \sigma_x, \quad (1)$$

where c is the biaxiality ratio in the elastic strain of the metal lattice and ν is the Poisson's ratio of the metal film (ν = 0.3). Equation (1) was derived from basic elasticity theory [96], assuming that the biaxiality ratio in the elastic strain of the metal lattice is equal to the global biaxiality ratio measured by total strain mapping (DIC) on the backside of the polymer at the yield point of the metal films of the specific sample considered. This assumption further entails pure elastic behavior and a good strain transmission at the interface. Combing the biaxial yield stress data with stress values obtained from polymer-supported uniaxial tensile tests on similar samples [26] we can attempt to calculate the complete biaxial stress dependence of plasticity of Al in our thin films and multilayers using the von Mises yield criterion (1913), similar to biaxial tensile tests with different applied load ratios reported in [65]. The calculated von Mises ellipses are shown in Fig. 6 for the four different film systems, including the two data points for the uni- and biaxial tensile tests with open and closed square symbols, respectively. Readers are reminded here that polymer-supported tensile tests of thin films are never purely uniaxial, as a result of the Poisson's ratio difference between film and substrate. The predicted purely uniaxial yield stresses (intercept of ellipse with x-axis) are included in Table 1 for film systems where our theory appears to be valid.

The unloading portions of the tensile tests, which are rarely reported, contain valuable compression data due to the continued elastic relaxation of the polymer substrate. Compressive yield strengths (0.2% and 0.02%) have been added to Fig. 6, for film systems that experience yield, as representative values to compare to the ellipse predictions in the compressive regime (bottom left quarter). Evidently, the films are compressed in a pre-deformed state following the tensile tests to obtain these values. Heavily cracked systems (uniaxial tensile tests to 12% strain [26]) have been excluded from this analysis, due to the difficulty of distin-

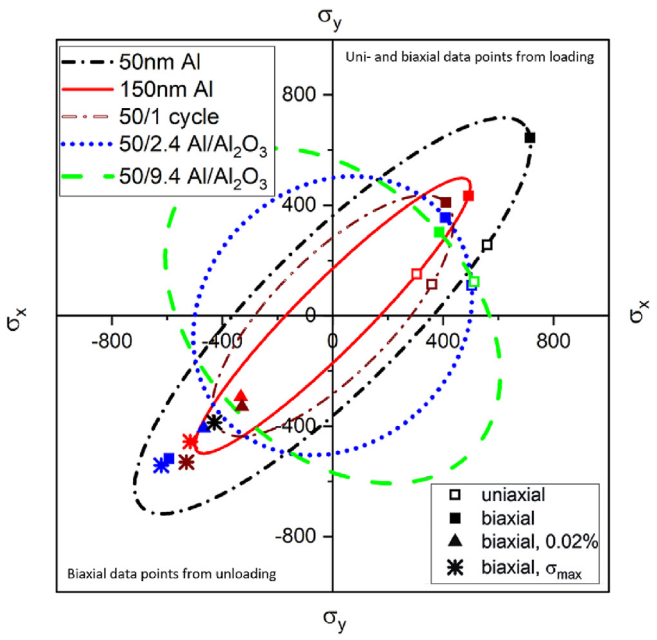

Fig. 6. Complete biaxial stress dependence of plasticity of Al/Al_2O_3 multilayers and reference Al films using the von Mises yield criterion. Two data points obtained from uni- and biaxial tensile tests on polymer substrates are included in the top right quarter with open and closed square symbols, respectively, for each sample. The maximum stress (Table 1) was used where this occurred below 0.2% plastic strain, otherwise a 0.2% yield stress was taken. Compressive 0.2% and 0.02% yield stresses as well as the maximum applied stress, σ_{max}, obtained from the unloading portion of the tensile experiments are included for comparison (bottom left quarter).

guishing between crack closure and plastic deformation during unloading. The full recovery of FWHM observed in biaxial tension ($\varepsilon_{max} \sim 3\%$) supports approximation of our films as "undeformed". Due to the intricacy of testing flexible thin films in compression the extracted values can still be considered meaningful points of reference. Unfortunately, the unloading portion of the 50/9.4 sample was lost and the scatter in the 50 nm Al data prohibited meaningful analysis. For the remaining samples, stabilizing of FWHM was used as a starting point for elastic loading during compression (grey Domain I, unloading Fig. 3). Compared to the loading case, only one film system (50/2.4) fulfilled the 0.2% yield criterion in compression due to the limited strain range. Further refinement of the yield criterion to 0.02% as suggested by Djaziri et al. [65] allows comparison to the remaining reference and multilayer film. Additionally, also the maximum stress reached during the unloading compression experiment was added for comparison with von Mises predictions, whereby sample to sample variation in σ_{max} are indicative of differences in the tensile induced defect density.

The overall shape of the ellipses obtained for the 50 nm and 150 nm Al films indicates that the von Mises theory is valid for pure Al. In both cases, the ellipses are elongated. Their aspect ratio, b/a, (a and b length of the major and minor ellipse axes) is calculated as 0.27 and 0.18 for 50 nm Al and 150 nm Al, respectively. Applying a similar yield criterion to the stress curves of 50 nm sputter-deposited Ni thin films on Kapton under different load ratios reported in literature [50], results in an ellipse with an aspect ratio of 0.40. Compared to this Ni study, there is greater ambiguity in our uniaxial data in determining the appropriate yield point because of the lower frequency of data point acquisition across the range of applied strain, potentially resulting in more elongated ellipses. For the multilayer sample consisting of three 50 nm Al layers separated by a single cycle of Al_2O_3 ALD cycle (50/1cycle) the ellipse is less elongated, with an aspect ratio of 0.37, which is closer to literature values for pure metal films [50]. The purpose of the single ALD cycle is to interrupt the Al microstructure in a controlled manner and produce 150 nm Al films with a 50 nm sublayer architecture. In uniaxial tension, this 50/1cycle film is distinctly weaker than a single 50 nm Al film but stronger than 150 nm Al (uniaxial σ_{max} values included in Table 1), leading to the conclusion that the free surface is an inefficient location for dislocation nucleation, or a poor sink [26]. With respect to the biaxial yield description, the predicted ellipse does not lie perfectly between 50 nm and 150 nm Al because the 50/1 cycle sample is the weakest of the three Al reference films in biaxial tension.

For the 50/2.4 sample, an even less elongated ellipse is predicted (blue curve, Fig. 5) with a higher aspect ratio of 0.86, which is beyond that of the 50/1cycle film and the Ni films [50], especially considering that our analysis method tends to underestimate the aspect ratio of the von Mises ellipse. It is unclear, whether in the high shear condition, which is along the short diagonal (top left to bottom right) Al will achieve the higher yield predicted by the ellipse or whether the failure of the oxide will become the limiting factor. Further work is necessary here to investigate the failure behavior of multilayers under such biaxial loading ratios. For the 50/9.4 sample the predicted ellipse is inverted (aspect ratio 1.44), suggesting that the von Mises criterion does not apply well, because incipient plastic yielding and subsequent cracking of the Al layers is too strongly influenced by the presence of the oxide layer and related heterogeneity effect of the microstructure in both quasi uni- and biaxial tension. Therefore, the von Mises yield criterion is not valid anymore. Alternatively, the Rankine criterion (1857), often used to predict fracture of brittle materials, could be applied, as proposed in Ref [65] for W/Cu nanocomposites.

Comparison of the ellipse prediction to the compression data obtained from the unloading segment of the tensile tests does not show very good agreement. Direct comparison of yield strength is difficult since a more refined yield criterion had to be applied to quantify/define yielding for the majority of the films within the limited strain range available, which is pre-defined by elastic properties of the polymer substrate. Generally, this measure causes experimental values to be lower than the von Mises prediction, which is observed for the 150 nm Al reference and the 50/1-cycle film. On the contrary, for the oxide-containing 50/2.4 multilayer, both the measured 0.02% and 0.2% yield stress exceed von Mises predictions based on tensile data. MD simulations of metal/ceramic Ti/TiN nanolaminates suggest two yield surfaces, associated to yielding of the metal and the ceramic layers, respectively, and a multiaxial tension/compression asymmetry with higher strength and ductility in compression [56]. Interestingly, the maximum compressive stress, σ_{max}, reached during unloading also significantly exceeded the von Mises prediction for the 50/1 cycle film.

It would certainly also be interesting to test our films deep in the high shear area ($\sigma_x = -\sigma_y$ regime) to understand that region better. The ability to accurately predict the full biaxial stress and failure dependence of a specific thin film material is also crucial if we consider the evolving variety of potential polymer substrates for flexible (electronics) applications, with each material combination resulting in a different biaxiallity ratio, depending on $\Delta\nu$. However, obtaining experimental data in the bottom right or top left quarter of the ellipse is difficult when working with thin films on polymer substrates, even considering biaxial tensile machines with four independent motors. Thicker polymer substrates could allow to apply a limited amount of compressive stress in one direction. Most polymers commonly used for flexible electronics applications have a Poisson's ratio in the range of 0.34–0.43 [97]. Changing to a polymer substrate with a lower Poisson's ratio compared to the metal film would also yield a limited range of additional data points. Conceptually, also changing the metal film can reverse the ratio of Poisson's contraction, however, is not feasible for the study of a specific thin film material such as Al/Al_2O_3, interesting for microelectronics. While currently there is no suitable polymer to suggest, another important factor to consider is efficient strain transfer between substrate and coating, governed by the metal-polymer interface. High interface strength can certainly be reached with carbonyl (C = O) containing options, forming an amorphous interlayer during thin film deposition [26,98].

5. Summary/Conclusions

Biaxial tensile straining with *in situ* XRD measurements was performed on unique Al/Al_2O_3 multilayers (PVD/ALD) and single layer Al reference films (PVD) deposited on flexible polymer substrates. Ultrathin Al_2O_3 layers (1 ALD cycle – 2.4 nm – 9.4 nm) are used to interrupt the out of plane grain growth of Al, generating an Al sublayer structure with columnar grains and a grain size well below the total film thickness. It was determined that the oxide layers decrease the yield strength and mechanically weaken the Al sublayers in biaxial tension, in contrast to strengthening effects observed during uniaxial polymer-supported loading. Biaxial XRD film stress and FWHM data are in good agreement with post-mortem SEM/FIB imaging regarding deformation of Al sublayers as a function of Al_2O_3 layer thickness, while finite element simulations highlight the importance of internal layer roughness. FWHM data proves particularly useful to decipher thickness dependent deformation of the ultrathin oxide layers, invisible to XRD themselves and extremely challenging to characterise mechanically in general. For multilayers with 9.4 nm Al_2O_3 layers (67 ALD cycles)

imposed fracture of Al sublayers occurs at ε_f = 2.2%, resulting in stress relaxation and a pronounced lateral 2D mud-crack pattern. With a reduced oxide thickness of 2.4 nm (17 ALD cycles) brittle cracking of Al can be avoided and the multilayers show improved crack resistance, as only scattered surface defects and no pronounced stress relaxation were observed within the applied strain range. Further cracking resistance in the film thickness direction is provided by fracture of individual sublayers while adjacent ones remain intact, while the formation of nanometre-sized holes at grain boundaries, a failure mechanism specific to the multilayers and the biaxial loading condition, has only a minor impact. Our attempt to describe the biaxial yield surface of the multilayers using both the loading (tensile) and unloading (compression) segments of the polymer supported tensile tests, demonstrates von Mises like behaviour for pure Al and up to 2.4 nm, whereby for the latter a significantly better performance in shear conditions is predicted, which remains challenging to prove experimentally.

Data availability

Data will be made available on request.

Declaration of Competing Interest

The authors declare that they have no known competing financial interests or personal relationships that could have appeared to influence the work reported in this paper.

Acknowledgements

SOLEIL is gratefully acknowledged for the beam time allocation (Proposal 20190179 and 20220220, DIFFABS beamline). B. P. and T. E.J.E. would like to acknowledge support from the EMPAPOSTDOCS-II program, which received funding from the European Union's Horizon 2020 research and innovation program under the Marie Skłodowska-Curie grant agreement number 754364. T.E.J.E. acknowledges funding from the European Union's Horizon 2020 research and innovation programme under the Marie Skłodowska-Curie grant agreement No. 840222. P-O. R. received support from the French Government Program "Investissements d'Avenir" (LABEX INTERACTIFS, ANR-11-LABX-0017-01 and, EUR INTREE, ANR-18-EURE-0010). Further support was provided by the Austrian Research Promotion Agency (FFG, grant number 857043).

Appendix A. Supplementary data

Supplementary data to this article can be found online at https://doi.org/10.1016/j.matdes.2023.112081.

References

[1] J. Azadmanjiri, C.C. Berndt, J. Wang, A. Kapoor, V.K. Srivastava, Nanolaminated composite materials: structure, interface role and applications, RSC Adv. 6 (2016) 109361–109385, https://doi.org/10.1039/c6ra20050h.
[2] C.D. Appleget, J.S. Riano, A.M. Hodge, An overview of nano multilayers as model systems for developing nanoscale microstructures, Materials (Basel) 15 (2022) 1–14, https://doi.org/10.3390/ma15010382.
[3] A. Misra, J.P. Hirth, R.G. Hoagland, Length-scale-dependent deformation mechanisms in incoherent metallic multilayered composites, Acta Mater. 53 (2005) 4817–4824, https://doi.org/10.1016/j.actamat.2005.06.025.
[4] S. Shen, H. Li, C. Wang, Y. Liang, N. Feng, N. Zhang, L. Yang, Mechanical properties and strengthening mechanism of Ni/Al nanolaminates: Role of dislocation strengthening and constraint in soft layers, Mater. Des. 226 (2023), https://doi.org/10.1016/j.matdes.2023.111632 111632.
[5] I. Salehinia, S. Shao, J. Wang, H.M. Zbib, Plastic deformation of metal/ceramic nanolayered composites, Jom. 66 (2014) 2078–2085, https://doi.org/10.1007/s11837-014-1132-7.
[6] Y. Ding, D.O. Northwood, A.T. Alpas, Fabrication of microlaminated Al/Al2O3 composites by magnetron sputtering for tribological applications, Surf. Coatings Technol. 62 (1993) 448–453, https://doi.org/10.1016/0257-8972(93)90282-S.
[7] J.-P. Niemelä, B. Putz, G. Mata-Osoro, C. Guerra-Nuñez, R.N. Widmer, N. Rohbeck, T.E.J. Edwards, M. Döbeli, K. Maćkosz, A. Szkudlarek, Y. Kuzminykh, X. Maeder, J. Michler, B. Andreaus, I. Utke, Mechanical properties of atomic-layer-deposited Al2O3/Y2O3 nanolaminate films on aluminum toward protective coatings, ACS Appl. Nano Mater. 5 (5) (2022) 6285–6296.
[8] N. Li, X.Y. Liu, Review: mechanical behavior of metal/ceramic interfaces in nanolayered composites—experiments and modeling, J. Mater. Sci. 53 (2018) 5562–5583, https://doi.org/10.1007/s10853-017-1767-1.
[9] Y. Kim, J. Lee, M.S. Yeom, J.W. Shin, H. Kim, Y. Cui, J.W. Kysar, J. Hone, Y. Jung, S. Jeon, S.M. Han, Strengthening effect of single-atomic-layer graphene in metal-graphene nanolayered composites, Nat. Commun. 4 (2013), https://doi.org/10.1038/ncomms3114.
[10] M. Ben Daia, P. Aubert, S. Labdi, C. Sant, F.A. Sadi, P. Houdy, J.L. Bozet, Nanoindentation investigation of Ti/TiN multilayers films, J. Appl. Phys. 87 (2000) 7753–7757, https://doi.org/10.1063/1.373450.
[11] S. Lotfian, C. Mayer, N. Chawla, J. Llorca, A. Misra, J.K. Baldwin, J.M. Molina-Aldareguía, Effect of layer thickness on the high temperature mechanical properties of Al/SiC nanolaminates, Thin Solid Films. 571 (2014) 260–267, https://doi.org/10.1016/j.tsf.2014.06.022.
[12] D. Bhattacharyya, N.A. Mara, P. Dickerson, R.G. Hoagland, A. Misra, A transmission electron microscopy study of the deformation behavior underneath nanoindents in nanoscale Al-TiN multilayered composites, Philos. Mag. 90 (2010) 1711–1724, https://doi.org/10.1080/14786430903459691.
[13] J.L. He, W.Z. Li, H.D. Li, C.H. Liu, Plastic properties of nano-scale ceramic – metal multilayers, Surf. Coatings Technol. 103-104 (1998) 276–280.
[14] S.A. Barnett, A. Madan, Hardness and stability of metal-nitride nanoscale multilayers, Scr. Mater. 50 (2004) 739–744, https://doi.org/10.1016/j.scriptamat.2003.11.042.
[15] G. Abadias, F. Pailloux, S.N. Dub, Epitaxial growth and mechanical properties of (001) ZrN/W nanolaminates, Surf. Coatings Technol. 202 (2008) 3683–3687, https://doi.org/10.1016/j.surfcoat.2008.01.013.
[16] T.E.J. Edwards, T. Xie, N.M. della Ventura, D. Casari, C. Guerra, E. Huszar, X. Maeder, J.J. Schwiedrzik, I. Utke, L. Pethö, J. Michler, On the thinnest Al2O3 interlayers in Al-based nanolaminates to enhance strength, and the role of constraint, Acta Mater. 240 (2022) 118345.
[17] L.W. Yang, C. Mayer, N. Chawla, J. Llorca, J.M. Molina-Aldareguía, Deformation mechanisms of ultra-thin Al layers in Al/SiC nanolaminates as a function of thickness and temperature, Philos. Mag. 96 (2016) 3336–3355, https://doi.org/10.1080/14786435.2016.1219075.
[18] S.B. Sinnott, E.C. Dickey, Ceramic/metal interface structures and their relationship to atomic- and meso-scale properties, Mater. Sci. Eng. R Reports 43 (2003) 1–59, https://doi.org/10.1016/j.mser.2003.09.001.
[19] J. Wang, A. Misra, Strain hardening in nanolayered thin films, Curr. Opin. Solid State Mater. Sci. 18 (2014) 19–28, https://doi.org/10.1016/j.cossms.2013.10.003.
[20] P.M. Anderson, C. Li, Hall-Petch relations for multilayered materials, Nanostructured Mater. 5 (1995) 349–362, https://doi.org/10.1016/0965-9773(95)00250-I.
[21] Y. Ding, Z. Farhat, D.O. Northwood, A.T. Alpas, Mechanical properties and tribological behaviour of nanolayered Al/Al2O3 and Ti/TiN composites, Surf. Coatings Technol. 68–69 (1994) 459–467, https://doi.org/10.1016/0257-8972(94)90202-X.
[22] E. Grossman, I. Gouzman, Space environment effects on polymers in low earth orbit, Nucl. Instrum. Methods Phys. Res. Sect. B Beam Interact. Mater. Atoms 208 (2003) 48–57, https://doi.org/10.1016/S0168-583X(03)00640-2.
[23] M. Hołyńska, A. Tighe, C. Semprimoschnig, Coatings and Thin Films for Spacecraft Thermo-Optical and Related Functional Applications, Adv. Mater. Interfaces 5 (2018) 1–20, https://doi.org/10.1002/admi.201701644.
[24] B. Hwang, W. Kim, J. Kim, S. Lee, S. Lim, S. Kim, S.H. Oh, S. Ryu, S.M. Han, Role of graphene in reducing fatigue damage in Cu/Gr nanolayered composite, Nano Lett. 17 (2017) 4740–4745, https://doi.org/10.1021/acs.nanolett.7b01431.
[25] E.J. Frankberg, J. Kalikka, F.G. Ferré, L. Joly-Pottuz, T. Salminen, J. Hintikka, M. Hokka, S. Koneti, T. Douillard, B. Le Saint, P. Kreiml, M.J. Cordill, T. Epicier, D. Stauffer, M. Vanazzi, L. Roiban, J. Akola, F. Di Fonzo, E. Levänen, K. Masenelli-Varlot, Highly ductile amorphous oxide at room temperature and high strain rate, Science (80-.) 366 (2019) 864–869, https://doi.org/10.1126/science.aav1254.
[26] B. Putz, T.E.J. Edwards, E. Huszar, P.A. Gruber, K.P. Gradwohl, P. Kreiml, D.M. Többens, J. Michler, Electromechanical behavior of Al/Al2O3 multilayers on flexible substrates: insights from in situ film stress and resistance measurements, Adv. Eng. Mater. (2022) 2200951. doi: 10.1117/12.733500.
[27] G. Abadias, C. Tromas, Y.Y. Tse, A. Michel, Investigation of the deformation behavior in nanoindented metal/nitride multilayers by coupling FIB-TEM and AFM observations, Mater. Res. Soc. Symp. Proc. 880 (2005) 41–46, https://doi.org/10.1557/proc-880-bb2.8/o3.8.
[28] H. Huang, F. Spaepen, Tensile testing of free-standing Cu, Ag and Al thin films and Ag / Cu multilayers, Acta Mater. 48 (12) (2000) 3261–3269.
[29] M.N. Polyakov, J. Lohmiller, P.A. Gruber, A.M. Hodge, Load sharing phenomena in nanoscale Cu/Nb multilayers, Adv. Eng. Mater. 17 (2015) 810–814, https://doi.org/10.1002/adem.201400368.

[30] K. Wu, J.Y. Zhang, J. Li, Y.Q. Wang, G. Liu, J. Sun, Length-scale-dependent cracking and buckling behaviors of nanostructured Cu/Cr multilayer films on compliant substrates, Acta Mater. 100 (2015) 344–358, https://doi.org/10.1016/j.actamat.2015.08.055.
[31] K. Wu, J.Y. Zhang, G. Liu, P. Zhang, P.M. Cheng, J. Li, G.J. Zhang, J. Sun, Buckling behaviors and adhesion energy of nanostructured Cu/X (X = Nb, Zr) multilayer films on a compliant substrate, Acta Mater. 61 (2013) 7889–7903, https://doi.org/10.1016/j.actamat.2013.09.028.
[32] M.J. Cordill, V.M. Marx, Fragmentation testing for ductile thin films on polymer substrates, Philos. Mag. Lett. 93 (2013) 618–624, https://doi.org/10.1080/09500839.2013.830792.
[33] O. Glushko, B. Putz, M.J. Cordill, Determining effective crack lengths from electrical measurements in polymer-supported thin films, Thin Solid Films 699 (2020), https://doi.org/10.1016/j.tsf.2020.137906 137906.
[34] F. Zighem, D. Faurie, A review on nanostructured thin films on flexible substrates: links between strains and magnetic properties, J. Phys. Condens. Matter. 33 (23) (2021) 233002.
[35] W. Dai, H. Xu, C. Zhang, Y. Li, H. Pan, H. Wang, G. Wei, X. Huang, Flexible magnetoelectrical devices with intrinsic magnetism and electrical conductivity, Adv. Electron. Mater. 5 (2019) 1–11, https://doi.org/10.1002/aelm.201900111.
[36] P.A. Gruber, J. Böhm, F. Onuseit, A. Wanner, R. Spolenak, E. Arzt, Size effects on yield strength and strain hardening for ultra-thin Cu films with and without passivation: A study by synchrotron and bulge test techniques, Acta Mater. 56 (2008) 2318–2335, https://doi.org/10.1016/j.actamat.2008.01.027.
[37] V.M. Marx, F. Toth, A. Wiesinger, J. Berger, C. Kirchlechner, M.J. Cordill, F.D. Fischer, F.G. Rammerstorfer, G. Dehm, The influence of a brittle Cr interlayer on the deformation behavior of thin Cu films on flexible substrates: Experiment and model, Acta Mater. 89 (2015) 278–289, https://doi.org/10.1016/j.actamat.2015.01.047.
[38] O. Kraft, M. Hommel, E. Arzt, X-ray diffraction as a tool to study the mechanical behaviour of thin films, Mater. Sci. Eng. A. 288 (2000) 209–216, https://doi.org/10.1016/S0921-5093(00)00876-5.
[39] P.A. Gruber, C. Solenthaler, E. Arzt, R. Spolenak, Strong single-crystalline Au films tested by a new synchrotron technique, Acta Mater. 56 (2008) 1876–1889, https://doi.org/10.1016/j.actamat.2007.12.043.
[40] J. Lohmiller, N.C. Woo, R. Spolenak, Microstructure-property relationship in highly ductile Au-Cu thin films for flexible electronics, Mater. Sci. Eng. A. 527 (2010) 7731–7740, https://doi.org/10.1016/j.msea.2010.08.043.
[41] J. Böhm, P. Gruber, R. Spolenk, A. Stierle, A. Wanner, E. Arzt, Tensile testing of ultrathin polycrystalline films: a synchrotron-based technique, Rev. Sci. Instrum. 75 (2004) 1110–1119, https://doi.org/10.1063/1.1669124.
[42] M.J. Cordill, F.D. Fischer, F.G. Rammerstorfer, G. Dehm, Adhesion energies of Cr thin films on polyimide determined from buckling: experiment and model, Acta Mater. 58 (2010) 5520–5531, https://doi.org/10.1016/j.actamat.2010.06.032.
[43] X.F. Zhu, B. Zhang, J. Gao, G.P. Zhang, Evaluation of the crack-initiation strain of a Cu-Ni multilayer on a flexible substrate, Scr. Mater. 60 (2009) 178–181, https://doi.org/10.1016/j.scriptamat.2008.10.004.
[44] O. Glushko, M.J. Cordill, A. Klug, E.J.W. List-Kratochvil, The effect of bending loading conditions on the reliability of inkjet printed and evaporated silver metallization on polymer substrates, Microelectron. Reliab. 56 (2016) 109–113, https://doi.org/10.1016/j.microrel.2015.10.007.
[45] X. Xian, Development of a bulge test experimental setup, 2015.
[46] B.E. Alaca, J.C. Selby, M.T.A. Saif, H. Sehitoglu, Biaxial testing of nanoscale films on compliant substrates: fatigue and fracture, Rev. Sci. Instrum. 73 (8) (2002) 2963–2970.
[47] J. Andersons, Y. Leterrier, Coating fragmentation by branching cracks at large biaxial strain, Probabilistic Eng. Mech. 22 (2007) 285–292, https://doi.org/10.1016/j.probengmech.2007.02.001.
[48] Y. Leterrier, D. Pellaton, D. Mendels, R. Glauser, J. Andersons, J.A.E. Månson, Biaxial fragmentation of thin silicon oxide coatings on poly(ethylene terephthalate), J. Mater. Sci. 36 (2001) 2213–2225, https://doi.org/10.1023/A:1017552302379.
[49] J. Andersons, Y. Leterrier, Advanced fragmentation stage of oxide coating on polymer substrate under biaxial tension, Thin Solid Films. 471 (2005) 209–217, https://doi.org/10.1016/j.tsf.2004.07.007.
[50] D. Faurie, F. Zighem, P. Godard, G. Parry, T. Sadat, D. Thiaudière, P.-O. Renault, In situ x-ray diffraction analysis of 2D crack patterning in thin films, Acta Mater. 165 (2019) 177–182, https://doi.org/10.1016/j.actamat.2018.11.040.
[51] S. Djaziri, P.O. Renault, F. Hild, E. Le Bourhis, P. Goudeau, D. Thiaudire, D. Faurie, Combined synchrotron X-ray and image-correlation analyses of biaxially deformed W/Cu nano-composite thin films on Kapton, J. Appl. Crystallogr. 44 (2011) 1071–1079, https://doi.org/10.1107/S0021889811030226.
[52] M.J. Cordill, P. Kreiml, B. Putz, D. Faurie, P.-O. Renault, D. Thiaudière, C. Mocuta, Role of layer order on the equi-biaxial behavior of Al/Mo bilayers, Scr. Mater. 194 (2021) 113656.
[53] J. Li, C. Li, L. Li, Q. Wang, Z. Wang, S. Wang, C. Sun, Study on fracture behavior in stiff-thin-film-on-soft-substrate structures under biaxial stress state, Int. J. Solids Struct. 219–220 (2021) 51–62, https://doi.org/10.1016/j.ijsolstr.2021.03.005.
[54] S. Van Petegem, A. Guitton, M. Dupraz, A. Bollhalder, K. Sofinowski, M.V. Upadhyay, H. Van Swygenhoven, A miniaturized biaxial deformation rig for in situ mechanical testing, Exp. Mech. 57 (2017) 569–580, https://doi.org/10.1007/s11340-016-0244-0.
[55] D.M. Collins, T. Erinosho, F.P.E. Dunne, R.I. Todd, T. Connolley, M. Mostafavi, H. Kupfer, A.J. Wilkinson, A synchrotron X-ray diffraction study of non-proportional strain-path effects, Acta Mater. 124 (2017) 290–304, https://doi.org/10.1016/j.actamat.2016.11.011.
[56] W. Yang, G. Ayoub, I. Salehinia, B. Mansoor, H. Zbib, Multiaxial tension/compression asymmetry of Ti/TiN nano laminates: MD investigation, Acta Mater. 135 (2017) 348–360, https://doi.org/10.1016/j.actamat.2017.06.034.
[57] E. Sacher, The present state of metallized polyimide, Mertallization Polym. (1990) 1–7, https://doi.org/10.1021/bk-1990-0440.ch001.
[58] F. Muktepavela, G. Bakradze, E. Tamanis, S. Stolyarova, N. Zaporina, Influence of mechanoactivation on the adhesion and mechanical properties of metal/oxide interfaces, Phys. Status Solidi C Conf. 2 (2005) 339–342, https://doi.org/10.1002/pssc.200460179.
[59] B. Putz, O. Glushko, V.M. Marx, C. Kirchlechner, D. Toebbens, M.J. Cordill, Electro-mechanical performance of thin gold films on polyimide, MRS Adv. 1 (12) (2016) 773–778.
[60] P.A. Gruber, E. Arzt, R. Spolenak, Brittle-to-ductile transition in ultrathin Ta/Cu film systems, J. Mater. Res. 24 (2009) 1906–1918, https://doi.org/10.1557/jmr.2009.0252.
[61] K. Zheng, C. Wang, Y.Q. Cheng, Y. Yue, X. Han, Z. Zhang, Z. Shan, S.X. Mao, M. Ye, Y. Yin, E. Ma, Electron-beam-assisted superplastic shaping of nanoscale amorphous silica, Nat. Commun. 1 (2010), https://doi.org/10.1038/ncomms1021.
[62] R.R. W, U.H. H, Corrosion and corrosion control - An Introduction to Corrosion Science and Engineering, 2008.
[63] J.D. Baran, H. Grönbeck, A. Hellman, Mechanism for limiting thickness of thin oxide films on aluminum, Phys. Rev. Lett. 112 (2014) 1–5, https://doi.org/10.1103/PhysRevLett.112.146103.
[64] A.T. Alpas, J.D. Embury, D.A. Hardwick, R.W. Springer, The mechanical properties of laminated microscale composites of Al/Al2O3, J. Mater. Sci. 25 (1990) 1603–1609, https://doi.org/10.1007/BF01045357.
[65] S. Djaziri, D. Faurie, P.-O. Renault, E. Le Bourhis, P.h. Goudeau, G. Geandier, D. Thiaudière, Yield surface of polycrystalline thin films as revealed by non-equibiaxial loadings at small deformation, Acta Mater. 61 (13) (2013) 5067–5077.
[66] T. Xie, T.E.J. Edwards, N.M. della Ventura, D. Casari, E. Huszár, L. Fu, L. Zhou, X. Maeder, J.J. Schwiedrzik, I. Utke, J. Michler, L. Pethö, Synthesis of model Al-Al2O3 multilayer systems with monolayer oxide thickness control by circumventing native oxidation, Thin Solid Films. 711 (2020) 138287.
[67] T. Li, Z. Suo, Ductility of thin metal films on polymer substrates modulated by interfacial adhesion, Int. J. Solids Struct. 44 (2007) 1696–1705, https://doi.org/10.1016/j.ijsolstr.2006.07.022.
[68] P.A. Gruber, A. Wanner, R. Spolenak, E. Arzt, Response to comment on: Size effects on yield strength and strain hardening for ultra-thin Cu films with and without passivation: A study by synchrotron and bulge test techniques, Scr. Mater. 67 (2012) 740–742, https://doi.org/10.1016/j.scriptamat.2012.07.005.
[69] E. Ma, Watching the nanograins roll, Science (80-.) 305 (5684) (2004) 623–624.
[70] J. Lohmiller, R. Baumbusch, O. Kraft, P.A. Gruber, Differentiation of deformation modes in nanocrystalline Pd films inferred from peak asymmetry evolution using in situ X-ray diffraction, Phys. Rev. Lett. 110 (2013) 1–5, https://doi.org/10.1103/PhysRevLett.110.066101.
[71] O. Kraft, P.A. Gruber, R. Mönig, D. Weygand, Plasticity in confined dimensions, Annu. Rev. Mater. Res. 40 (2010) 293–317, https://doi.org/10.1146/annurev-matsci-082908-145409.
[72] M.J. Cordill, P. Kreiml, B. Putz, C. Trost, A. Lassnig, C. Mitterer, D. Faurie, P.-O. Renault, Film thickness and architecture effects in biaxially strained polymer supported Al/Mo bilayers, Mater. Today Commun. 31 (2022) 103455.
[73] D.S. Herman, M.A. Schuster, R.M. Gerber, Hillock growth on vacuum deposited aluminum films, J. Vac. Sci. Technol. 9 (1972) 515–519, https://doi.org/10.1116/1.1316673.
[74] F. Ericson, N. Kristensen, J.Å. Schweitz, U. Smith, A transmission electron microscopy study of hillocks in thin aluminum films, J. Vac. Sci. Technol. B Microelectron. Nanom. Struct. 9 (1991) 58–63, https://doi.org/10.1116/1.585790.
[75] B.C. Martin, C.J. Tracy, J.W. Mayer, L.E. Hendrickson, A comparative study of Hillock formation in aluminum films, Thin Solid Films. 271 (1995) 64–68, https://doi.org/10.1016/0040-6090(95)06941-0.
[76] B. Putz, S. Wurster, T.E.J. Edwards, B. Völker, G. Milassin, D.M. Többens, C.O.A. Semprimoschnig, M.J. Cordill, Mechanical and optical degradation of flexible optical solar reflectors during simulated low earth orbit thermal cycling, Acta Astronaut. 175 (2020) 277–289, https://doi.org/10.1016/j.actaastro.2020.05.032.
[77] W.M. Mook, R. Raghavan, J.K. Baldwin, D. Frey, J. Michler, N.A. Mara, A. Misra, Indentation fracture response of Al–TiN Nanolaminates, Mater. Res. Lett. 1 (2013) 102–108, https://doi.org/10.1080/21663831.2013.783515.
[78] M.P. de Boer, A.D. Corwin, P.G. Kotula, M.S. Baker, J.R. Michael, G. Subhash, M.J. Shaw, On-chip laboratory suite for testing of free-standing metal film mechanical properties, Part II – Experiments, Acta Mater. 56 (2008) 3313–3326, https://doi.org/10.1016/j.actamat.2008.03.034.
[79] S.H. Oh, M. Legros, D. Kiener, G. Dehm, In situ observation of dislocation nucleation and escape in a submicrometre aluminium single crystal, Nat. Mater. 8 (2009) 95–100, https://doi.org/10.1038/nmat2370.
[80] V. Rontu, A. Nolvi, A. Hokkanen, E. Haeggström, I. Kassamakov, S. Franssila, Elastic and fracture properties of free-standing amorphous ALD Al2O3 thin

films measured with bulge test, Mater. Res. Express. 5 (2018), https://doi.org/10.1088/2053-1591/aabbd5.
[81] D.S. Gianola, D.H. Warner, J.F. Molinari, K.J. Hemker, Increased strain rate sensitivity due to stress-coupled grain growth in nanocrystalline Al, Scr. Mater. 55 (2006) 649–652, https://doi.org/10.1016/j.scriptamat.2006.06.002.
[82] M.N. Giovan, G. Sines, Biaxial and uniaxial data for statistical comparisons of a ceramic's strength, J. Am. Ceram. Soc. 62 (1979) 510–515, https://doi.org/10.1111/j.1151-2916.1979.tb19117.x.
[83] S.H. Oh, C. Rentenberger, J. Im, C. Motz, D. Kiener, H.P. Karnthaler, G. Dehm, Dislocation plasticity of Al film on polyimide investigated by cross-sectional in situ transmission electron microscopy straining, Scr. Mater. 65 (2011) 456–459, https://doi.org/10.1016/j.scriptamat.2011.06.001.
[84] D.C. Agrawal, R. Raj, Measurement of the ultimate shear strength of a metal-ceramic interface, Acta Metall. 37 (1989) 1265–1270, https://doi.org/10.1016/0001-6160(89)90120-X.
[85] D.L. Rode, V.R. Gaddam, J.H. Yi, Subnanometer surface roughness of dc magnetron sputtered Al films, J. Appl. Phys. 102 (2) (2007) 024303.
[86] B. Putz, C. May-Miller, V. Matl, B. Völker, D.M. Többens, C. Semprimoschnig, M. J. Cordill, Two-stage cracking of metallic bi-layers on polymer substrates under tension, Scr. Mater. 145 (2018) 5–8, https://doi.org/10.1016/j.scriptamat.2017.09.039.
[87] P. Gruber, J. Böhm, A. Wanner, L. Sauter, R. Spolenak, E. Arzt, Size effect on crack formation in Cu/Ta and Ta/Cu/Ta thin film systems, MRS Proc. 821 (2004) 1–7, https://doi.org/10.1557/proc-821-p2.7.
[88] P.G. and D.T. G. Geandier, L. Gélébart, O. Castelnau, E. Le Bourhis, P.-O. Renault, Micromechanical Modeling of the Elastic Behavior of Multilayer Thin Films; Comparison with In Situ Data from X-Ray Diffraction, IUTAM Symp. Model. Nanomater. Nanosyst. (2009). doi: 10.1007/978-1-4020-9557-3.
[89] S. Lee, H. Ghaffarian, W. Kim, T. Lee, S.M. Han, S. Ryu, S.H. Oh, A study on dislocation mechanisms of toughening in cu-graphene nanolayered composite, Nano Lett. 22 (2022) 188–195, https://doi.org/10.1021/acs.nanolett.1c03599.
[90] E.J. Patiño, N.G. Kelkar, Experimental determination of tunneling characteristics and dwell times from temperature dependence of Al/Al2O3/Al junctions, Appl. Phys. Lett. 107 (2015) 1–5, https://doi.org/10.1063/1.4938209.
[91] V.D. Das, M.S. Jagadeesh, Tunneling in Al/Al2O3/Al MIM structures, Phys. Status Solidi. 66 (1981) 327–333, https://doi.org/10.1002/pssa.2210660140.
[92] M. Koberidze, M.J. Puska, R.M. Nieminen, Structural details of Al/Al2O3 junctions and their role in the formation of electron tunnel barriers, Phys. Rev. B 97 (2018), https://doi.org/10.1103/PhysRevB.97.195406.
[93] L. Fry-Bouriaux, M.C. Rosamond, D.A. Williams, A.G. Davies, C. Wälti, Field-enhanced direct tunneling in ultrathin atomic-layer-deposition-grown Au-Al2O3 -Cr metal-insulator-metal structures, Phys. Rev. B 96 (2017) 1–11, https://doi.org/10.1103/PhysRevB.96.115435.
[94] T.O. Kääriäinen, D.C. Cameron, Plasma-assisted atomic layer deposition of Al2O3 at room temperature, Plasma Process. Polym. 6 (S1) (2009) S237–S241.
[95] M.D. Groner, F.H. Fabreguette, J.W. Elam, S.M. George, Low-Temperature Al2O3 Atomic Layer Deposition, Chem. Mater. 16 (2004) 639–645, https://doi.org/10.4313/teem.2003.4.3.015.
[96] V. Molotnikov, A. Molotnikova, Theory of Elasticity and Plasticity, Springer-Verlag, 2021.
[97] http://polymerdatabase.com/polymer%20physics/Poisson%20Table.html, (n.d.).
[98] L. Atanasoska, S.G. Anderson, H.M. Meyer III, Z. Lin, J.H. Weaver, Aluminum / polyimide interface formation : An xray photoelectron spectroscopy study of selective chemical bonding, J. Vac. Sci. Technol. A 5 (1987) 3325–3333, https://doi.org/10.1116/1.574191.